Article

Current Biology

# Non-centrosomal microtubules at kinetochores promote rapid chromosome biorientation during mitosis in human cells

## Graphical abstract

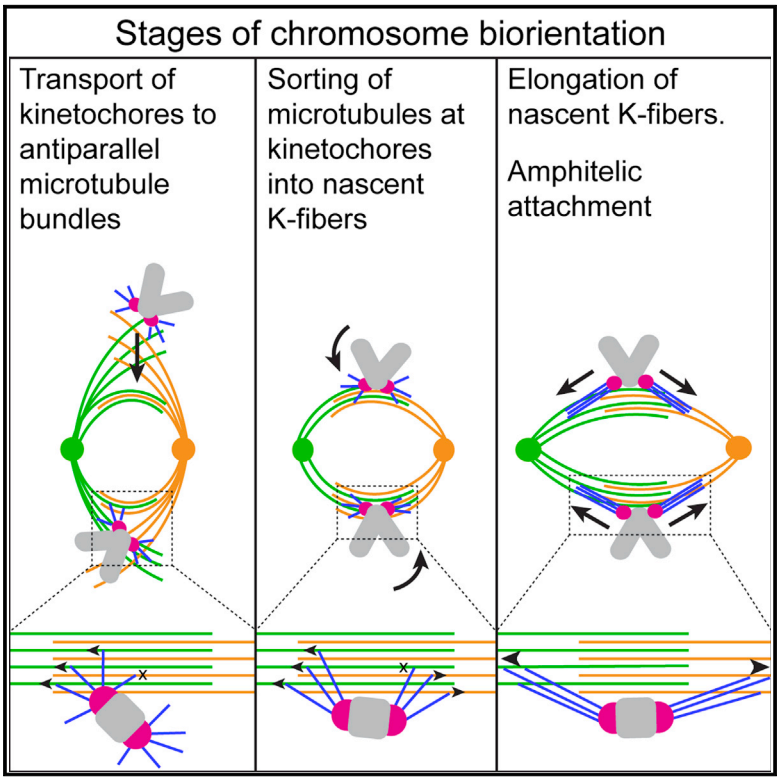


## Authors

Fioranna Renda, Christopher Miles, Irina Tikhonenko, ..., Tarun M. Kapoor, Alex Mogilner, Alexey Khodjakov

## Correspondence

mogilner@cims.nyu.edu (A.M.), alexey.khodjakov@health.ny.gov (A.K.)

## In brief

Based on analyses of chromosome behavior in human cells and computational modeling, Renda et al. propose a mechanism for synchronous attachment of sister kinetochores to the opposite spindle poles via dynamic interactions between short non-centrosomal microtubules at the kinetochore and bundles of antiparallel microtubules within the spindle.

## Highlights

- Amphitelic attachments form synchronously at a specific stage of spindle elongation
- Amphitelic attachments form within a spatial domain defined by microtubule bundles
- Bundles of antiparallel microtubules facilitate chromosome biorientation
- CenpE and dynein at kinetochore affect the efficiency and rapidity of biorientation

Renda et al., 2022, Current Biology *32*, 1049–1063
March 14, 2022 
https://doi.org/10.1016/j.cub.2022.01.013

CellPress

Current Biology

CellPress

Article

# Non-centrosomal microtubules at kinetochores promote rapid chromosome biorientation during mitosis in human cells

Fioranna Renda,[1,6] Christopher Miles,[2,3,6] Irina Tikhonenko,[1] Rebecca Fisher,[1] Lina Carlini,[4] Tarun M. Kapoor,[4] Alex Mogilner,[2,*] and Alexey Khodjakov[1,5,7,*]

[1]Wadsworth Center, New York State Department of Health, Albany, NY, USA
[2]Courant Institute and Department of Biology, New York University, New York, NY, USA
[3]Department of Mathematics and the NSF-Simons Center for Multiscale Cell Fate Research, University of California, Irvine, Irvine, CA, USA
[4]Laboratory of Chemistry and Cell Biology, Rockefeller University, New York, NY, USA
[5]Biological Sciences, Rensselaer Polytechnic Institute, Troy, NY, USA
[6]These authors contributed equally
[7]Lead contact
*Correspondence: mogilner@cims.nyu.edu (A.M.), alexey.khodjakov@health.ny.gov (A.K.)
https://doi.org/10.1016/j.cub.2022.01.013

## SUMMARY

Proper segregation of chromosomes during mitosis depends on "amphitelic attachments"—load-bearing connections of sister kinetochores to the opposite spindle poles via bundles of microtubules, termed as the "K-fibers." Current models of spindle assembly assume that K-fibers arise largely from stochastic capture of microtubules, which occurs at random times and locations and independently at sister kinetochores. We test this assumption by following the movements of all kinetochores in human cells and determine that most amphitelic attachments form synchronously at a specific stage of spindle assembly and within a spatially distinct domain. This biorientation domain is enriched in bundles of antiparallel microtubules, and perturbation of microtubule bundling changes the temporal and spatial dynamics of amphitelic attachment formation. Structural analyses indicate that interactions of kinetochores with microtubule bundles are mediated by non-centrosomal short microtubules that emanate from most kinetochores during early prometaphase. Computational analyses suggest that momentous molecular motor-driven interactions with antiparallel bundles rapidly convert these short microtubules into nascent K-fibers. Thus, load-bearing connections to the opposite spindle poles form simultaneously on sister kinetochores. In contrast to the uncoordinated sequential attachments of sister kinetochores expected in stochastic models of spindle assembly, our model envisions the formation of amphitelic attachments as a deterministic process in which the chromosomes connect with the spindle poles synchronously at a specific stage of spindle assembly and at a defined location determined by the spindle architecture. Experimental analyses of changes in the kinetochore behavior in cells with perturbed activity of molecular motors CenpE and dynein confirm the predictive power of the model.

## INTRODUCTION

For proper segregation during mitosis, each chromosome must "biorient"—physically connect with both poles of the mitotic "spindle," a macromolecular machine that self-assembles from microtubules (MTs). Load-bearing attachments of chromosomes to MTs are mediated by the kinetochores (KTs), a pair of macromolecular complexes on opposite sides of the chromosome's centromere. The goal of spindle assembly is to attach sister KTs to the opposite spindle pole ("amphitelic attachment"). Current models of spindle assembly stem from the "search & capture" (S&C) hypothesis,[1] which envisions the formation of amphitelic attachments via sequential capture of MTs emanating from the opposite spindle poles by the sister KTs. This stochastic process is facilitated by localized nucleation of MTs near chromosomes,[2–4] guidance of MT growth toward KTs,[5–8] stabilization of the initial connections,[9] and regulation of KT architecture.[10–13] Even with these facilitations, random discovery of sister KTs is expected to yield variable duration of spindle assembly and frequent errors arising from accidental capture of MTs produced by a "wrong" spindle pole.[2,14–17] These expectations seem to be in contrast with the rapid and robust cell division observed in chromosomally stable cells.

Here, we analyze KT behavior and MT organization to determine when, where, and how amphitelic attachments form during mitosis in diploid human cells. We find that, within a cell, chromosomes biorient synchronously at a defined stage of spindle elongation and within a spatially distinct "biorientation domain" of the spindle. Computational analyses suggest that amphitelic attachments form in a single step via dynamic motor-mediated interactions between short MTs protruding from sister KTs and bundles of antiparallel MTs within the biorientation domain.

Experimental perturbations of MT bundling or motor activities at the KTs change the dynamics of chromosome biorientation in a manner consistent with the model predictions. Thus, simultaneous connection of sister KTs to bundles of antiparallel MT is likely a major mechanism for chromosome biorientation in chromosomally stable human cells.

## RESULTS

### Amphitelic attachments form predominantly at a specific stage of spindle elongation

We follow the movements of KTs in chromosomally stable human RPE1 cells in 3D at 5-s intervals. To minimize stress from fluorescence microscopy, we tag KTs and centrioles in the same color[18,19] and discriminate these organelles by their behavior (Figure 1A; Video S1). Under these conditions, RPE1 cells initiate anaphase 23 ± 3 min (n = 17) after nuclear envelope breakdown (NEB) and show no chromosome mis-segregation as expected for normal mitosis.[10,19]

Two direct consequences of amphitelic attachment are a decrease in the angle between the line connecting sister KTs (i.e., centromere axis) and the line connecting spindle poles (i.e., spindle axis), as well as an increase in the distance between sister KTs (Figure S1A; cTilt and IKD). Consistent with previous reports,[19] we observe that the mean value of cTilt decreases, whereas the mean IKD increases during the first 8 min of prometaphase in the population of 17 cells (Figure 1B; 784 chromosomes). However, significant variability exists in the dynamics of cTilt and IKD among individual cells. In some cells, these metrics change rapidly and plateau ~ 6 min after NEB (Figure 1C). In other cells, the changes are delayed for several minutes (Figure 1D).

Euploid cells remain in mitosis until all the chromosomes become bioriented and, therefore, IKD and cTilt values observed just prior to anaphase onset (AO) characterize a pool of chromosomes with >99% amphitelic attachments. We reason that, when both IKD and cTilt of a chromosome converge within one SD from the mean pre-AO values (Figure S1B), the chromosome has formed amphitelic attachments. Specifically, we probe trajectories of sister KTs for the time point when IKD exceeds 0.9 μm while cTilt remains below ~22.5° ($\pi/8$) for at least 30 s (Figure S1C). By these conservative criteria, 763 of 784 chromosomes (97.3%) in the 17 analyzed cells achieve biorientation <15 min after NEB, with the maximal probability of forming amphitelic attachments ~6 min after NEB (Figure 1E). However, temporal distributions of biorientation events vary significantly among individual cells. In some cells, most chromosomes biorient <4 min after NEB (Figure 1F, median). In other cells, amphitelic attachments form en masse >8 min after NEB (Figure 1G). Biorientations occur earlier in cells where the spindle elongates to its full length rapidly (compare "Cell1" and "Cell2" in Figures 1C, 1D, and 1F–1H). This observation prompted us to test whether the peak of biorientation events coincides with a specific stage of spindle elongation. For this purpose, we normalize progression through prometaphase by the duration of spindle elongation (0 = NEB, 1 = time point when spindle elongation stops; STAR Methods). On the "spindle elongation time" (SET) scale, biorientation peaks coincide in various cells, and the distribution of biorientation events in the population is narrow and nearly normal (Figures 1I–1K). Thus, the majority of amphitelic attachments form during a short interval when the spindle reaches ~80% of its maximum length, irrespective of when this stage of spindle assembly occurs in physical time. These data suggest that the state of the spindle determines when most chromosomes become bioriented.

### Amphitelic attachments form rapidly near bundles of microtubules

To determine the trigger of amphitelic attachment formation, we imaged SiR-Tubulin[20] in cells with GFP-tagged KTs and centrioles. Spindle architecture and duration of mitosis are normal in cells followed at 30-s intervals (Video S2), which is sufficient for observing the behavior of centromeres during the formation of amphitelic attachments.

Recordings of 18 cells suggest that amphitelic attachments form when a KT encounters a bundle of MTs. Within a minute after the initial contact with a bundle, the centromere stretches to >0.9 μm and its axis aligns with the bundle (Figures 2A and 2B). To estimate the frequency of contacts between KTs and MT bundles, we analyzed the 3D distribution of spindle components in fixed prometaphase cells. MT bundles are detected via immunostaining for PRC1, a MT-associated protein known to bundle antiparallel MTs.[21–24] In RPE1 cells, PRC1 decorates a subset of MTs throughout prometaphase (Figure S2A), and a similar pattern is observed in cells that express a full-length PRC1-GFP fusion (Figure S2B). In cells with ~12 μm spindles, which corresponds to ~80% of the full length and, therefore, to the stage of spindle elongation when most amphitelic attachments form (Figure 1), PRC1-decorated bundles form a barrel around the spindle axis (Figure 2C), and the KTs are adjacent to the bundles (Figure 2D; mean distance of 0.44 ± 0.24 μm, 909 KTs in 11 cells).

To detail the interaction between KTs and MT bundles, we employ array tomography[25] (AT). A higher signal/noise ratio of AT reveals locations of short MTs that escape detection in conventional fluorescence microscopy.[26,27] Analysis of 5 prometaphase cells confirms the presence of MT bundles arranged in a ring and oriented roughly parallel to the spindle axis (Figure 2E). KTs reside near (~500 nm), yet are not directly attached to, these bundles. Instead, small tubulin spots bridge the Hec1-containing outer KT and the adjacent bundle (Figure 2F). Similar tubulin spots have been reported to contain variable numbers of short non-centrosomal MTs in correlative LM/EM analysis of early prometaphase RPE1 cells.[26]

Our observation that amphitelic attachments form rapidly near MT bundles prompted us to explore whether the time and place of amphitelic attachment formation change under conditions that perturb bundling of MTs within the spindle. Toward this goal, we introduced an inducible shRNA construct against PRC1 to RPE1 cells with GFP-tagged KTs and centrioles (STAR Methods). Consistent with previous reports, cells depleted of PRC1 progress through mitosis;[28,29] however, the central spindle that normally comprises MT bundles is not present during telophase (Figures S2C and S2D). For reproducibility, only cells that display this phenotype are included in our analyses (STAR Methods).

Depletion of PRC1 does not significantly change the shape and dimensions of the spindle (Figure 3A); however, MTs are

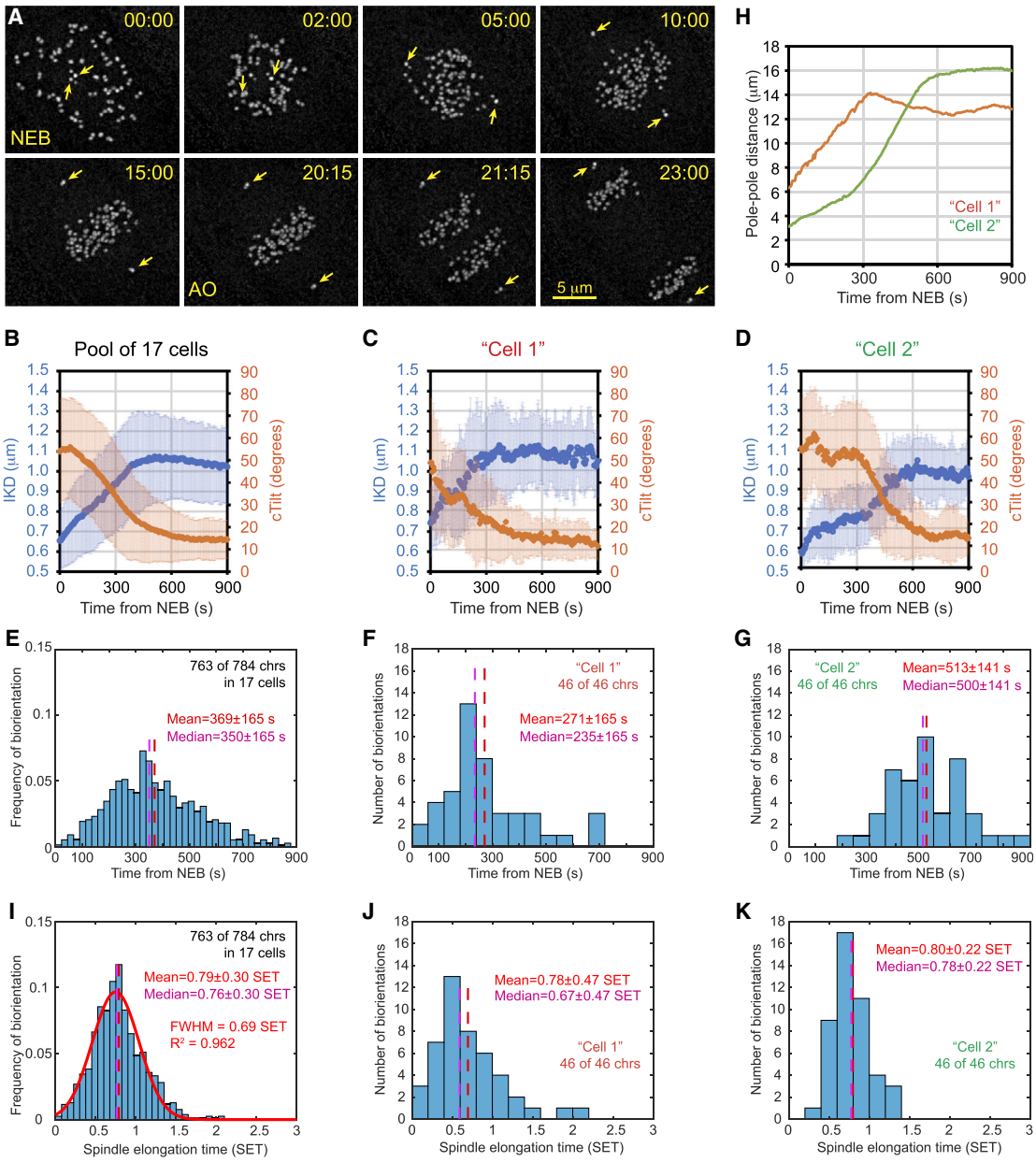


**Figure 1. Amphitelic attachments form at a specific stage of spindle elongation**

(A) Selected time points from a recording of mitosis in RPE1 cell at 5-s intervals. Frames are maximum-intensity projections of the entire cell. KTs and centrioles are tagged with CenpA-GFP and Centrin1-GFP. Arrows mark centrioles. Nuclear envelope breaks down at 00:00 (NEB) and anaphase onsets at 20:15 (AO). Scale bar, 5 µm.

(B) Dynamics of the distance between sister KTs (IKD, blue) and angle between the centromere axis and spindle axis (cTilt, orange) for 784 KTs in 17 cells.

(C and D) Similar to (B), but the plots present two selected cells. Images of Cell1 are shown in (A).

(E) Temporal distribution of biorientation events in the population of 17 cells.

(F and G) Similar to (E), but the plots present two selected cells.

(H) Dynamics of spindle length in the two selected cells.

(I) As in (E), but time is normalized by the duration of spindle elongation (SET) for each cell in the population. Notice that the distribution is nearly normal (red line).

(J and K) As in (F) and (G), but time is expressed in SET.

Error bars in (B)–(D) are standard deviation. See also Figure S1 and Video S1.

distributed in a more homogeneous pattern within the spindle and the ring of MT bundles is not present during mid-prometaphase (Figure 3B; compare with Figure 2D).

In ~75% of RPE1 cells, the centrosomes reside on the dorsal and ventral surfaces of the nucleus at NEB.[19,30] As the spindle elongates during prometaphase, its axis reorients from nearly

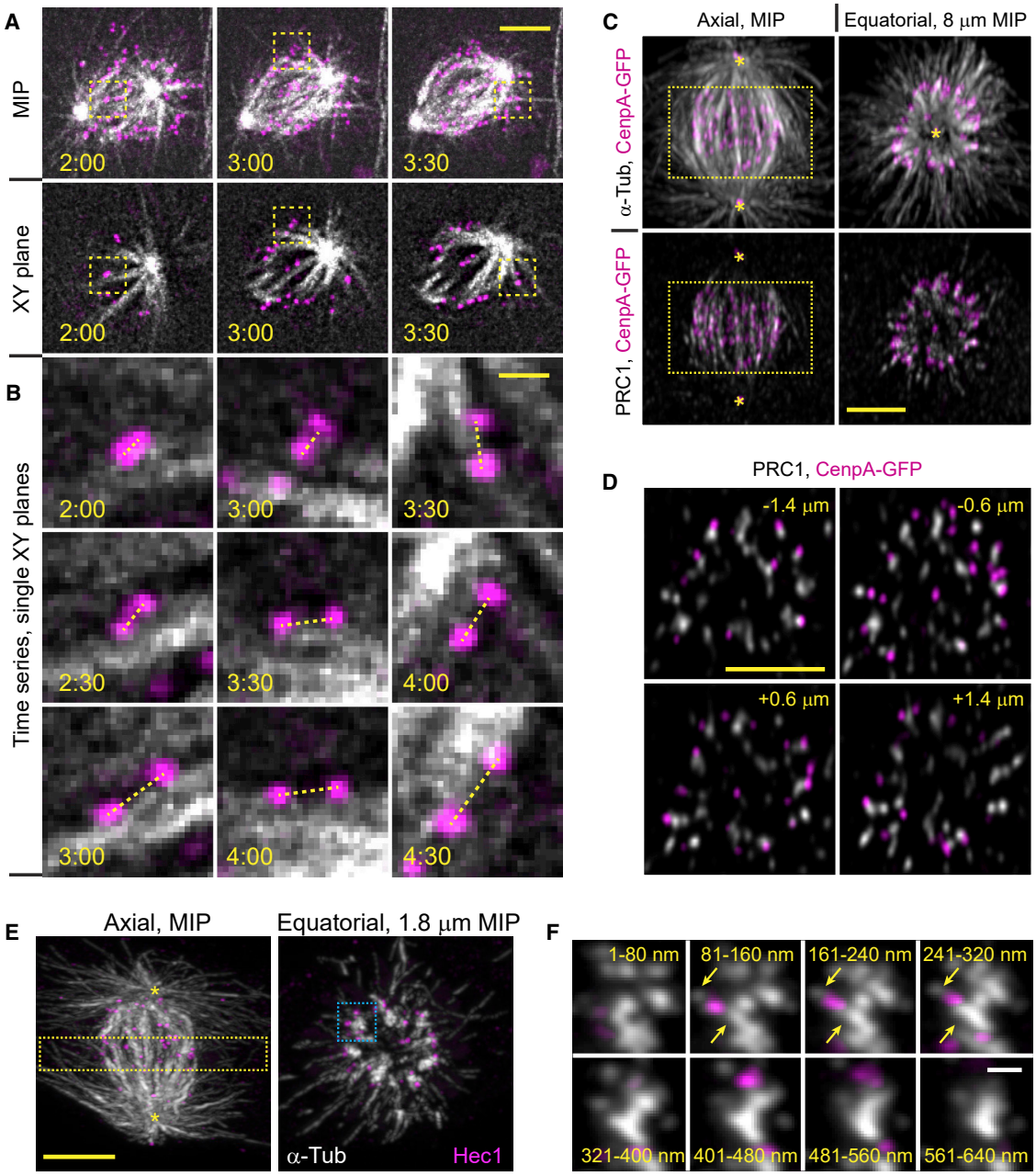


**Figure 2. Amphitelic attachments form near microtubule bundles**

(A) Selected time points from a recording of RPE1 cell with GFP-tagged KTs and centrioles (shown in magenta) and SiR-tubulin-labeled MTs (shown in grayscale). Maximum-intensity projections (top row) and selected single planes (bottom row) are shown for each time point.

(B) Biorientation behavior of three KTs marked with boxes in (A). Notice that centromeres abruptly orient parallel to a MT bundle and stretch within 1 min after the initial contact with this bundle.

(C) Spatial arrangement of MTs (α-tubulin), MT bundles (PRC1), KTs (CenpA-GFP), and centrioles (Ctn1-GFP) in a prometaphase cell with ~12 μm long spindle. Axial view is a maximum-intensity projection of the entire spindle. Equatorial view presents a partial volume denoted by the box in axial view. Asterisks denote centrioles.

(D) Individual equatorial planes from the volume shown in (C). Distance from each plane to the spindle equator is shown.

(E) Similar to (C), but this volume is constructed from a series of 80-nm sections (array tomography) and KTs are visualized via immunostaining for Hec1.

(F) Sequential tomography slices detailing MT distribution near KTs marked with the blue box in (E). Arrows denote α-tubulin spots between KTs and MT bundles. Scale bars, 5 μm in (A) and (C)–(E), 1 μm in (B), and 0.5 μm in (F). Asterisks mark positions of spindle poles. See also Figure S2 and Video S2.

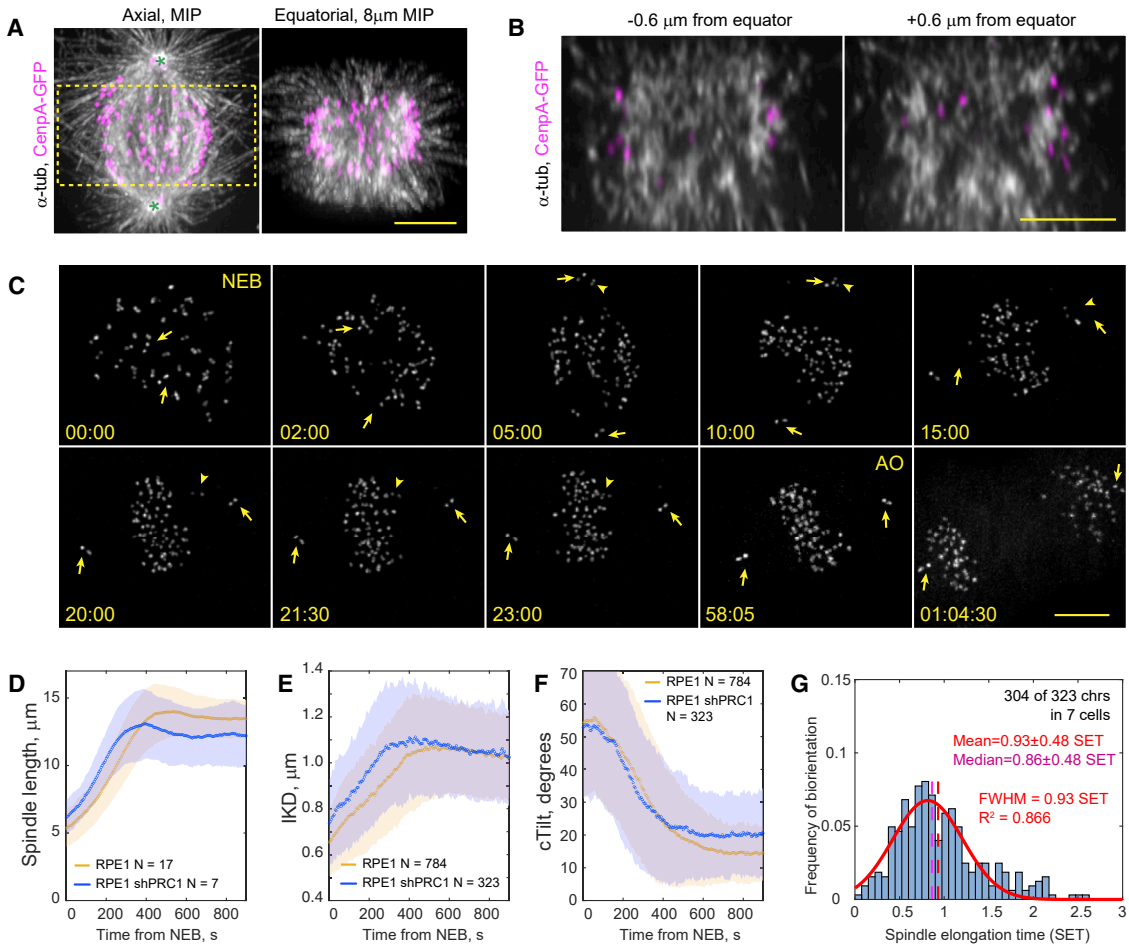


**Figure 3. Lack of microtubule bundles delays formation of amphitelic attachments**

(A) Spatial arrangement of MTs (α-tubulin), KTs (CenpA-GFP), and centrioles (Ctn1-GFP) in a prometaphase shRNA depleted of PRC1. Axial view is a maximum-intensity projection of the entire spindle. Equatorial view presents a partial volume denoted by the box in axial view. Asterisks denote centrioles (~12 μm spindle length).

(B) Individual equatorial planes from the from the volume shown in (A).

(C) Selected time points from a recording of PRC1-depleted RPE1 cell with GFP-tagged KTs and centrioles. Frames are maximum-intensity projections of the entire cell. Nuclear envelope breaks down at 00:00 (NEB) and anaphase onsets at 58:05 (AO). Arrows mark centrioles, arrowheads mark a mono-oriented chromosome.

(D–F) Dynamics of mean spindle length (D), distance between sister KTs (E, IKD), and the angle between the centromere and spindle axes (F, cTilt). Colored corridors are ±1 SD.

(G) Temporal distribution of biorientation events in PRC1-depleted cells, normalized to spindle elongation time. Notice significant deviation from the normal distribution (red line).

Scale bars, 5 μm in (A)–(C). See also Figures S2 and S3 and Video S3.

orthogonal to nearly parallel to the coverslip surface (Figure 1A). This pattern, as well as the rate of spindle elongation, are similar in PRC1-depleted cells (Figures 3C and 3D; Video S3). The mean distance between sister KTs (IKD) in PRC1-depleted cells increases faster during early prometaphase; however, it plateaus at the same level as in the wild-type (WT) RPE1 (Figure 3E). Orientation of centromeres (cTilt) improves similarly in control versus PRC1-depleted cells during earlier prometaphase. However, the mean value plateaus at a higher level, and the SD is twice as large in the latter (Figure 3F; $p < 0.001$, Student's t test). The increased SD reflects instability in the orientation of individual centromeres that often "tumble" repeatedly after a brief period of proper alignment. PRC1-depleted cells often display mono-oriented chromosomes that ultimately congress onto the metaphase plate prior to anaphase (Figure 3C). Consistent with the notion that mono-oriented chromosomes prevent mitotic exit,[31] both the mean and variability of mitotic duration increase significantly in PRC1 cells (37 ± 10 min, n = 30 versus 23 ± 3 min, n = 17 in the WT RPE1; $p < 0.001$, Student's t test).

Formation of amphitelic attachments in PRC1-depleted cells is delayed, with both the mean and median values significantly larger than in WT RPE1 (Figure 3G; $p < 0.0001$, Kruskal-Wallis test). The temporal distribution of biorientation events is positively skewed with many chromosomes achieving the amphitelic state during late prometaphase (Figure 3G; compare

with Figure 1I). Thus, perturbation of MT bundling within the spindle impedes the normal dynamics of chromosome biorientation.

## Microtubule bundles delineate a spatial domain that promotes chromosome biorientation

To determine where within the spindle the majority of amphitelic attachments form and how the chromosomes reach their biorientation locales, we analyzed centromere trajectories prior to and post biorientation of each chromosome. Extensive rotations and positional shifts of the spindle during prometaphase obscure centromere movements plotted in the conventional Cartesian coordinates linked to the microscope stage (Figure S3A). We overcome this problem by expressing positions in a spindle-centric cylindrical coordinate system (Figure S3A′; STAR Methods), which allows us to view trajectories from fixed relative viewpoints, specifically in axial and equatorial projections (Figures S3B and S3D).

Prior to biorientation, centromeres rapidly and linearly move toward the center of the spindle (Figure S3B). The linear inward movements stop abruptly when centromeres arrive at 2.5–3.5 μm from the spindle axis and within ~3 μm from the equator (Figure S3B). Upon arrival to this part of the spindle, IKD and cTilt exceed the biorientation thresholds and the centromere begins to move roughly parallel to the spindle axis, as expected for bioriented chromosomes (Figure S3B′). The abrupt change in the motion pattern is consistent with the rapid formation of amphitelic attachments upon contact with a MT bundle (Figure 2B). To assess the spatial distribution of biorientation events in multiple cells with variable dimensions of the spindle, we normalize distances by the maximal spindle length (MSL) achieved in each cell at the end of spindle elongation. This approach demonstrates that amphitelic attachments form predominantly within a doughnut (toroid) around the spindle axis (Figure 4A), with a mean equatorial radius of 0.23 MSL, thickness of the wall of 0.19 MSL, and an axial length of 0.32 MSL (Figure S3C; 763 biorientations in 17 cells).

The rapid inward movement of centromeres during early prometaphase persists in cells depleted of PRC1. However, the centromeres do not display the abrupt change in the motion pattern typical for the WT RPE1. Instead, after the rapid delivery to within ~3.5 μm from the spindle axis, the centromeres drift in both axial and equatorial directions for variable times, which is manifested as jitter in the late segments of pre-biorientation trajectories (Figure S3D). These movements convert into a more regular axial motion (Figure S3D′) after the IKD and cTilt values exceed their biorientation thresholds. Formation of amphitelic attachments occurs within a large volume within the spindle (Figure 4B), and the distribution of biorientation events in the equatorial plane deviates from the normal distribution observed in the WT RPE1 (Figure S3E; compare with Figure S3C). Thus, the sharply delineated barrel-shaped domain that promotes chromosome biorientation in the WT RPE1 cells (Figure 4A) disintegrates when MT bundling is perturbed via depletion of PRC1 (Figure 4B).

The dimensions of the spindle as well as its shape change as the cell progresses through prometaphase, and thus the volume enriched in MT bundles is not constant. To delineate the shape of the biorientation domain at various stages of spindle assembly, we employ constitutive expression of a GFP-tagged full-length PRC1 in RPE1 cells. At a moderate expression level, the localization of this construct (Figure S2B) is similar to the distribution of endogenous PRC1 (Figure S2A). Furthermore, cells that express GFP-PRC1 progress through mitosis at a normal pace and segregate chromosomes properly (Video S4).

Live-cell recordings demonstrate that within the first 30 s of prometaphase, PRC1-GFP is recruited to a subset of irregularly oriented MTs (Video S4). Within ~4 min, as the spindle elongates to ~0.8 of its maximum length, these MTs organize into a hollow barrel-shaped array roughly parallel to the spindle axis (Figure 4C; Video S4). To reveal the typical shape of the PRC1-GFP distribution, we averaged recordings of 12 cells with dimensions normalized by MSL. The edge of the PRC1-enriched domain (Figure 4D) resembles the shape of a chain hung from two posts, which prompted us to approximate this edge by a catenary function with coefficients proportional to the spindle length (STAR Methods). We find that over half of centromeres reside <0.85 μm from the catenary at the time point when IKD and cTilt exceed their biorientation thresholds, irrespective of whether this occurs during earlier or later prometaphase (Figure 4E). Furthermore, we find that ~94% of centromeres approach closer than 0.85 μm from the catenary prior to their biorientation.

To detail the interactions between MTs and KTs adjacent to MT bundles, we employed correlative light/electron microscopy (LM/EM) in RPE1 cells expressing PRC1-GFP. Analysis of two prometaphase cells with ~12 μm spindles (~0.8 MSL) demonstrates the presence of short (300–600 nm) MTs that bridge the KT plates with bundles of 10–15 PRC1-decorated MTs (Figure 4F). These observations are consistent with the previous report that KTs residing on the spindle surface are end-on attached to numerous short non-centrosomal MTs that emanate from the KT and intermix with the spindle MTs.[26]

## Computational model of biorientation on bundled antiparallel microtubules

Our observations suggest that during normal mitosis, amphitelic attachments form rapidly within a defined spatial domain where short MTs emanating from the KTs encounter MT bundles decorated with PRC1. Previous investigations identified multi-valent complexes of the minus-end-directed molecular motor dynein and NuMA as the linkers that connect the minus ends of MTs protruding from KTs to the adjacent MT bundles and forcefully pull KTs poleward.[27,32–34] These findings prompted us to computationally explore whether motor-mediated interactions between the minus ends of disorganized MTs emanating from the KT (Figure 5A) and bundles of antiparallel MT bundles within the spindle provide an efficient means for rapid biorientation. We developed a stochastic spatial mechanical model in which sister KTs are the ends of the centromeric spring (Figure 5B). Short MTs randomly pivot around their plus ends anchored at the sister KTs when dyneins at their minus ends are unbound from the long spindle MTs. Binding can occur when short MT minus ends are near a long spindle MT. While bound, dyneins pull the short MT minus ends toward the long MT minus ends. Between these kinetic events, the positions of the KTs evolve via forces mediated through bound short MTs (see Methods S1 for further details and mathematics of the model). Intuitively, stochastic dynein-mediated connections at the short MT ends emanating from the KTs in various directions (Figure 5A) would jerk the

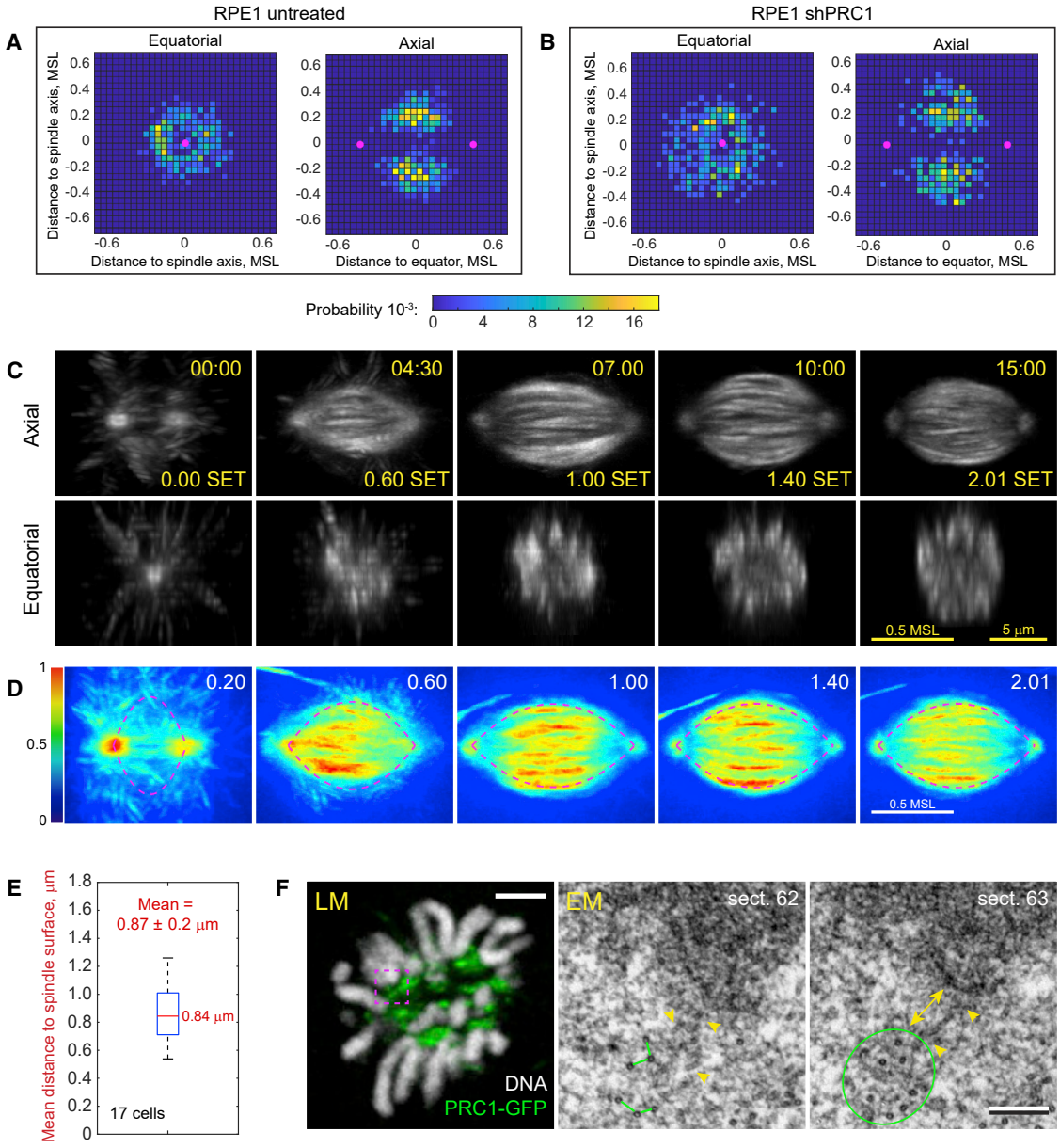


**Figure 4. Amphitelic attachments form within a spindle domain enriched in microtubule bundles**

(A and B) Spatial distribution of biorientation events in the untreated (A) and PRC1-depleted (B) cells. 2D histograms in the equatorial and axial planes are shown. Distances are normalized to the maximal spindle length in each cell. Magenta dots denote positions of spindle poles at the time with maximum probability of biorientation.

(C) Selected time points from a timelapse recording of mitosis in RPE1 cells expressing PRC1-GFP. Axial and equatorial maximum-intensity projections of 3D volumes are shown. The volumes are aligned at each time point to stabilize the spindle position and orientation. Timestamps are in min:s after NEB and in fraction of spindle elongation time (SET). Scale bars are 5 μm and 0.5 of the maximal spindle length (MSL) reached in this cell.

(D) Average of 3D time lapse recordings aligned as in (A) and spatially normalized by the maximal spindle length in each cell. Color map encodes intensity of PRC1-GFP in the averaged volume. Dashed lines approximate the edge of PRC1-enriched domain by an empirically constructed catenary function (STAR Methods). Timestamps are in SET. Scale bar is 0.5 MSL.

(E) Tukey's boxplot of Euclidian distances from centromeres to the catenary (edge of PRC1-enriched domain) at the time of amphitelic attachment formation. Mean value is reported with SD.

(F) Typical arrangement of microtubules near kinetochores adjacent to PRC1-decorated bundles. LM—a single-plane image depicting PRC1-GFP (green) and chromosomes (Hoechst 33342, grayscale) in a fixed cell. EM—80-nm serial sections through the area boxed in LM. Kinetochore plate is ~250 nm (yellow double arrow) from the edge of a bundle comprising 10 microtubules (green circle) with 50–70-nm spacing between individual microtubules (green lines). Short microtubules (arrowheads) bridge the bundle and the kinetochore plate. Scale bars, 3 μm (LM) and 200 nm (EM).

See also Video S4.

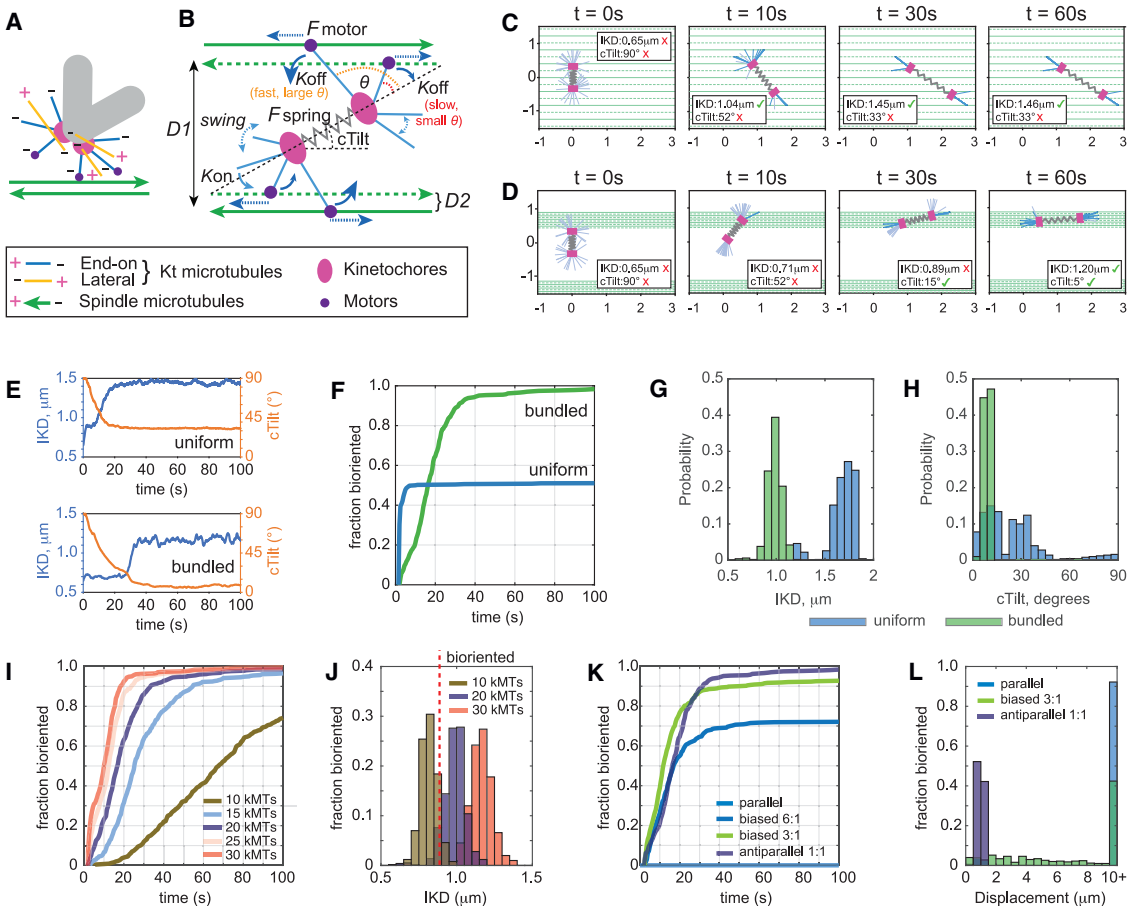


**Figure 5. Computational model of chromosome biorientation**

(A) MT arrangement at the KTs considered in the model. Only MTs with the plus end attached to the KT and the minus end protruding outwards (blue lines) contribute to the interaction with the spindle. This interaction is mediated by a minus end-directed motor (dynein, purple dots).

(B) Principal framework of the model. Protruding KT MTs pivot around the KTs until their minus ends connect to the walls of reachable spindle MTs with rate defined by $K_{on}$ when in proximity. Once connected, the minus end attempts to move along the spindle MT toward its minus end. Connections of MTs protruding from sister KTs to spindle MTs of opposite polarity stretch the centromere and increase the longevity of the connection by decreasing the rate $K_{off}$ via their spatial organization. Orientation of the spindle MTs is intermittent, and their organization is characterized by the distances *D1* and *D2*. See supplemental information for details.

(C–E) Examples of behavior predicted for centromeres (single simulation run). (C) On spindle surface comprising evenly spaced (D1 = D2 = 200 nm distance) MTs of intermittent polarity, the centromere stretches but fails to orient along the spindle axis.

(D) On spindle surface comprising MT bundles separated by D1 = 2 μm (10 MTs of intermittent polarity, D2 = 50 nm), the centromere orients and stretches to the level expected for bioriented chromosomes.

(E) Dynamics of IKD and cTilt for centromeres shown in (C) and (D).

(F) Fraction of centromeres predicted to achieve biorientation at various times for the evaluated scenarios.

(G and H) Predicted distributions of IKD and cTilt after 100 s of interaction with the spindle surface comprising evenly spaced individual MTs (blue) versus MT bundles (green).

(I) Fraction of bioriented centromeres for various numbers of MT minus ends protruding from the KT.

(J) Distributions of IKD predicted for various numbers of MT minus ends after 100 s of interaction with MT bundles.

(K) Fraction of bioriented centromeres for various ratios of MTs with the opposite polarity. Notice that biorientation fails on parallel MT bundles (light blue).

(L) Predicted displacement from the point of initial contact toward the bundle terminus with the greater number of minus ends for bundles with various polarity bias (100 s of interaction, 20 MTs protruding from the kinetochore).

See also Video S5.

KTs around and lead to unstable cTilt and low IKD values. However, we establish numerically that a simple assumption leads to a different outcome: if the rate of the short-long MT unbinding is lower when short MTs are pulled in the directions that are more parallel to the centrosomal axis (Figure 5B), then the following geometric-mechanical positive feedback ensues. Even when the centromere axis is initially perpendicular (Figure 5C; t = 0 s) to the long MTs, the random forces from dynein tilt the axis (Figure 5C; t = 10 s). Then, the short MTs that are oriented more parallel to the centrosomal axis are bound stably, whereas the short MTs that are oriented more normal to the centrosomal axis unbind rapidly, swing, and rebind; hence, ultimately, most of the short MTs from each KT bind only to those long MTs that lead the short MT minus ends in the same direction to which

the KT is tilted (Figure 5C; t = 30 s). This MT polarity sorting resulting from the dynein motors' tug-of-war aligns the centromere with the spindle MTs (which decreases cTilt). The improvement in centromere orientation further increases the disparity between the oppositely pulling short MTs, so the initially disorganized array of short MTs protruding from the KT transforms into a bundle of parallel MTs, and the forces acting along these "nascent K-fibers" stretch the centromere (increasing IKD).

Our assumption of differences in the stability of motor-mediated MT interactions is supported by the observations of increased detachment rates under higher angles between the pulling force vector and the track of molecular motors.[35,36] Furthermore, the notion that pulling sister KTs toward the opposite spindle poles stabilizes MT attachments is generally accepted.[37–41]

To test the feasibility of rapid biorientation via interaction between the short MTs at KTs and the spindle, we ran a series of computational simulations based on the rules and forces presented in Figure 5B (see Methods S1 for parameters). First, we explore whether the proposed mechanism depends on the distribution of long MTs within the spindle and, more specifically, whether the surface of the spindle comprises a uniform array of evenly spaced individual MTs versus a series of MT bundles (Figures 5C–5E). We find that centromeres interacting with a surface of evenly spaced antiparallel MTs stretch rapidly because short MTs find many long MTs to attach to and pull along. However, these interactions fail to orient the centromere parallel to the spindle axis because the randomly selected long MTs, along which the short MTs pull, could be widely separated (Figure 5C; Video S5). In contrast, a centromere that interacts with a bundle comprising ~10 antiparallel MTs at ~50 nm spacing, which resembles the configuration observed by correlative LM/EM (Figure 4F), both stretches and orients parallel to the bundle (Figure 5D; Video S5). Within ~100 s from the onset of the interaction, virtually all modeled centromeres on a bundle reach the values of IKD and cTilt expected for bioriented chromosomes. In contrast, only about 50% of centromeres on a uniform MT surface satisfy both biorientation criteria (Figure 5F). Interestingly, interactions with the surface of individual MTs are predicted to stretch the centromere to a greater extent than interactions with a bundle (Figure 5G). The model also predicts a greater variability in cTilt angles for centromeres that interact with individual MTs (Figure 5H). These predictions are consistent with the dynamics of IKD and cTilt values observed in the WT versus PRC1-depleted cells that lack MT bundles (Figure 3).

Exploration of the model by parameter sweeps identifies two factors that are important for rapid and efficient biorientation. First, the process depends on the number of MT minus ends protruding from the KT when it encounters a bundle. Whereas KTs with >20 attached MTs biorient efficiently, the time required for the formation of amphitelic attachments increases rapidly for <10 attached MTs (Figure 5I). The delay arises because KTs with a lower number of attached microtubules fail to stretch the centromere above the biorientation threshold after 100 s of interaction (Figure 5J). Conversely, centromeres with 30 or more attached MTs tend to over-stretch (Figure 5J). Thus, ~20 MT minus ends protruding from the KT are optimal for biorientation. This number is consistent with the number of short MTs detected in EM reconstructions of KTs positioned on the spindle surface in early prometaphase RPE1 cells.[26] Second, an important determinant of biorientation efficiency is the ratio of MTs with opposite polarity within the bundle. When the polarity bias exceeds 3:1, many centromeres fail to form amphitelic attachments in a reasonable time (Figure 5K). Furthermore, dynein-mediated interactions with a polarity-biased bundle are predicted to shift the centromere from the place of the initial encounter toward the terminus of the bundle with the higher number of MT minus ends. In the context of the spindle, this means that interactions with polarity-biased microtubules promote chromosome mono-orientation (Figure 5L). Thus, rapid formation of amphitelic attachments is predicted to be most efficient near the spindle equator, where polarity bias within the bundles is expected to be minimal.

## Changes in chromosome behavior upon inactivation of microtubule motors at the kinetochore are consistent with the model prediction

The model predicts that rapid formation of amphitelic attachments occurs when centromeres with an optimal number of short MTs attached to sister KTs promptly gather within the biorientation domain enriched in MT bundles. Thus, perturbation of MT bundling, delayed delivery of centromeres to the bundle-enriched domain, or an insufficient number of MT minus ends protruding from the KT would all affect the temporal and spatial distributions of biorientation events. Consistent with the model prediction, we observe a delayed and less synchronous formation of amphitelic attachments within a larger volume when MT bundling is inhibited via PRC1 depletion (Figures 4A and 4B). To test whether abnormal transport of centromeres to the biorientation domain or a lower number of MT minus ends protruding from sister KTs yields effects that are consistent with the model, we perturb the activities of molecular motors CenpE (kinesin 7) or cytoplasmic dynein at the KT. Chemical inhibition of CenpE has been shown to decrease the number of short MTs end-on attached to KTs during early prometaphase,[26] likely due to the role of this motor in the conversion from lateral to end-on interactions with captured MTs.[42] Dynein has been implicated in the transport of chromosomes toward the spindle during prometaphase.[43–45] Thus, KTs lacking this motor are likely to encounter MT bundles at a later stage of spindle assembly.

A cell permeable inhibitor, GSK923295, offers an efficient means of inhibiting CenpE activity.[46] To assess the role of dynein at the KT, we employed RPE1 cells with genetically ablated Rod, an adapter protein required for the recruitment of dynein to KTs.[12,47,48] Inhibition of CenpE or failure to recruit dynein to the KTs neither noticeably affects the spindle architecture (Figure S4A) nor changes the pattern of spindle orientation or the rate of spindle elongation during prometaphase (Figure S4B). However, the dynamics of chromosome biorientation change prominently in these cells, as evident from changes in the dynamics of cTilt and IKD (Figures S4C and S4D). Mono-oriented chromosomes, remaining near a spindle pole for an extended time, are commonly observed (Figures 6A and 6B; Videos S6 and S7). Although many chromosomes reside closer to one spindle pole (<0.25 of the contemporary spindle length) at NEB, linear movements toward the spindle center (Figure S3B′) rapidly decrease the number of these initially mono-oriented

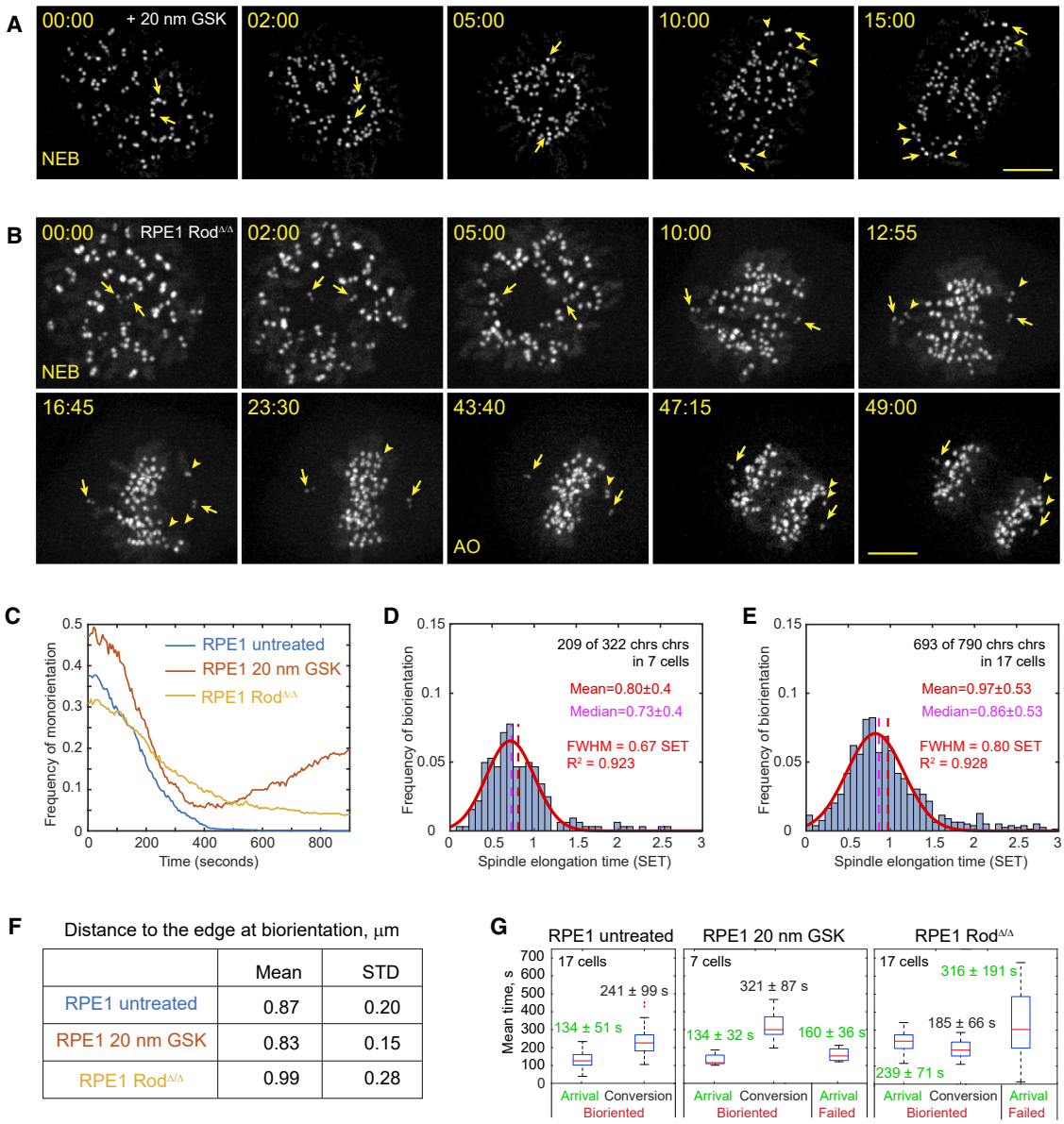


**F** Distance to the edge at biorientation, μm

| | Mean | STD |
|---|---|---|
| RPE1 untreated | 0.87 | 0.20 |
| RPE1 20 nm GSK | 0.83 | 0.15 |
| RPE1 Rod$^{\Delta/\Delta}$ | 0.99 | 0.28 |




**Figure 6. Dynamics and localization of amphitelic attachment formation in cells lacking activities of CenpE or dynein at the kinetochore**

(A and B) Selected time points from recording of mitosis in the WT RPE1 cell treated with 20 nM GSK923295 (A) or RPE1 Rod$^{\Delta/\Delta}$ (B). KTs and centrioles are tagged with CenpA-GFP and Centrin1-GFP. Arrows denote centrioles. Arrowheads point at KTs on mono-oriented chromosomes. Scale bar, 5 μm.

(C) Fraction of chromosomes with centromeres residing <0.25 of the spindle length from a pole (i.e., mono-oriented).

(D and E) Temporal distribution of biorientation events (normalized by spindle elongation time) in cells lacking activity of CenpE (D) or dynein at the KT (E).

(F) Mean and SD values for distances from centromeres to the edge of the bundle-enriched spindle domain during formation of amphitelic attachments.

(G) Tuckey's box plots for times when centromeres arrive within 0.85 μm from the edge of the bundle-enriched domain (Arrival) and intervals from the arrival to the formation of amphitelic attachments (Conversion). Arrival times of centromeres that formed amphitelic attachments and centromeres that fail to biorient in the first 15 min of prometaphase are reported separately. Mean values are reported with SD.

See also Figure S4 and Videos S6 and S7.

chromosomes in the untreated RPE1 (Figure 6C). In CenpE-inhibited cells, the number of mono-oriented chromosomes decreases similarly during the first 400 s of prometaphase, but subsequently it increases (Figure 6C) as many chromosomes move toward the spindle center in early prometaphase and then migrate along the spindle axis toward a spindle pole (Figures 6C and S4E). In contrast, the number of mono-oriented chromosomes in Rod$^{\Delta/\Delta}$ RPE1 declines slowly but steadily throughout prometaphase, as shown in Figure 6C. The slower decline correlates with the lack of rapid centripetal movements of centromeres during early prometaphase (Figure S4F). Peripheral chromosomes in Rod$^{\Delta/\Delta}$ gradually migrate closer to the spindle axis and the equator via directionally unstable movements (Figure S4F).

Consistent with the observation of persistent mono-orientation, ~37% (119/321) chromosomes in CenpE-inhibited and ~13% (97/790) chromosomes in Rod$^{\Delta/\Delta}$ cells fail to form amphitelic attachments within 15 min after NEB. However, temporal dynamics of biorientation are markedly different in CenpE-inhibited versus Rod$^{\Delta/\Delta}$ cells (Figures 6D and 6E). In the former, although a lower number of chromosomes achieve biorientation, most amphitelic attachments form at the same stage of spindle elongation as in untreated RPE1 (0.80 ± 0.40 SET versus 0.79 ± 0.30 SET; compare Figures 1I and 6D; $p = 0.7179$, Kruskal-Wallis test). In Rod$^{\Delta/\Delta}$ cells, formation of amphitelic attachments is delayed (0.97 ± 0.53 SET; compare Figures 1I and 6E; $p < 0.0001$, Kruskal-Wallis test) and the distribution is skewed with many chromosomes achieving biorientation during late prometaphase (Figure 6E). Slower biorientation in Rod$^{\Delta/\Delta}$ is consistent with longer and more variable duration of mitosis (41 ± 15 min, n = 17 versus 23 ± 3 min, n = 17 in the WT RPE1; Student's t test, $p < 0.001$).

As in untreated RPE1 cells, the formation of amphitelic attachments in both CenpE-inhibited and Rod$^{\Delta/\Delta}$ cells occurs predominantly within the spatial domain delineated by the same catenary function as in the WT RPE1 cells. Only insignificant differences are detected in the mean distance from the centromere to the catenary at the time of biorientation (Figure 6F). In contrast, the number of centromeres that do not enter the biorientation domain (remain >0.85 μm to the catenary throughout prometaphase) increases from ~6% in the WT (48/784) and CenpE-inhibited (21/321) cells to ~18% in Rod$^{\Delta/\Delta}$ (140/790). Importantly, the number of chromosomes that fail to form amphitelic attachments is significantly higher among those that do not enter the biorientation domain (53%).

To assess the efficiency of amphitelic attachment formation near MT bundles, we analyzed when centromeres enter the biorientation domain and the interval from their arrival to the formation of amphitelic attachment (Figure S4G). The mean arrival times in the untreated versus CenpE-inhibited cells do not differ significantly irrespective of whether the chromosome subsequently forms amphitelic attachments (Figure 6G). However, the interval from the arrival to amphitelic attachment formation is significantly longer in CenpE-inhibited cells. In Rod$^{\Delta/\Delta}$ cells, arrival to the biorientation domain is significantly delayed, particularly for the chromosomes that fail to form amphitelic attachments (Figure 6G). In contrast, the interval from the arrival to amphitelic attachments formation is shorter in Rod$^{\Delta/\Delta}$ cells (Figure 6G). Thus, consistent with the model predictions, a lower number of MTs at the KT has no effect on the timely delivery of centromeres to the biorientation domain near the spindle equator; however, these centromeres often fail to form amphitelic attachments and subsequently shift poleward. In contrast, lack of dynein at the KT interferes with the delivery of centromeres to the biorientation domain but does not decrease the efficiency of amphitelic attachment formation on centromeres that encounter MT bundles.

## DISCUSSION

We propose a mechanism for the synchronous formation of load-bearing connections of sister kinetochores to the opposite spindle poles (Figure 7). In contrast to the random sequential attachment of sister kinetochores envisioned in models based on the S&C hypothesis,[9,49–54] our model predicts almost instantaneous formation of amphitelic attachments on centromeres delivered to the biorientation domain of the spindle. Thus, proper architecture of the spindle determines where and when chromosomes achieve biorientation. Significant changes in the dynamics and spatial distribution of biorientation events in cells under conditions that interfere with various aspects of the proposed mechanism suggest that it is a major contributor during normal mitosis.

A key feature of our model is that load-bearing connections are formed by KTs that are already attached to the plus ends of short non-centrosomal MTs (Figure 7). The presence of these MTs at most KTs during the earliest stages of spindle formation has been demonstrated[26,55,56] and incorporation of MTs nucleated at the KT into K-fibers appears to continue throughout mitosis.[57] Live-cell microscopy demonstrates that MTs that are nucleated at KT develop into bundles that grow outward and eventually connect to the spindle poles.[27,32,33,58,59] However, how the initial array of MTs at the KT converts into a K-fiber with proper polarity is unknown. Our model suggests that efficient sorting of MTs into two bundles that are oriented toward the opposite spindle poles arises from transient interactions between MTs protruding from the KTs and bundles of antiparallel MTs. A key prediction is that a low number of minus ends protruding from the KT slow the conversion (Figure 5I), which is consistent with the increased conversion time in CenpE-inhibited cells (Figure 6G), where the number of protruding MTs is lower.[26]

Consistent with the proposed model, amphitelic attachments form over a longer period and within a greater volume in cells depleted of PRC1, where bundles of antiparallel MTs are scarce. However, all the chromosomes in these cells eventually biorient, and thus, proximity to antiparallel bundles is not essential. Indeed, our model predicts that sorting of short MTs also occurs on the surface comprising antiparallel individual MTs, although the efficiency is reduced (Figure 5F). Interestingly, centromeres are overstretched during early prometaphase in PRC1-depleted cells (Figure 3E), consistent with the model predictions. Alternatively, spindle assembly in the absence of MT bundles may occur primarily via conventional S&C. Several features of mitosis in PRC1-depleted cells are consistent with this possibility. First, the temporal distribution of biorientation is positively skewed with a tail, indicating that a fraction of KTs is captured only after a very long and variable time as expected in stochastic S&C.[49] Second, centromeres in PRC1-depleted cells exhibit extended poleward movements (Figure S3D) and a higher frequency of mono-orientation as expected for uncoordinated attachments of sister kinetochores. Irrespective of the mechanism(s) that allow amphitelic attachments to form under abnormal conditions, our data indicate that most amphitelic attachments arise near antiparallel bundles when the bundles are accessible. This notion gains further support from the association of mature K-fibers with PRC1-decorated MT bundles of MTs that "bridge" K-fibers of sister kinetochores in various cell types.[23,24,60–62]

Our current computational analyses quantitatively address only the mechanism of centromere biorientation upon arrival to the spindle surface. The preceding step, centripetal convergence of the peripheral chromosomes, requires additional

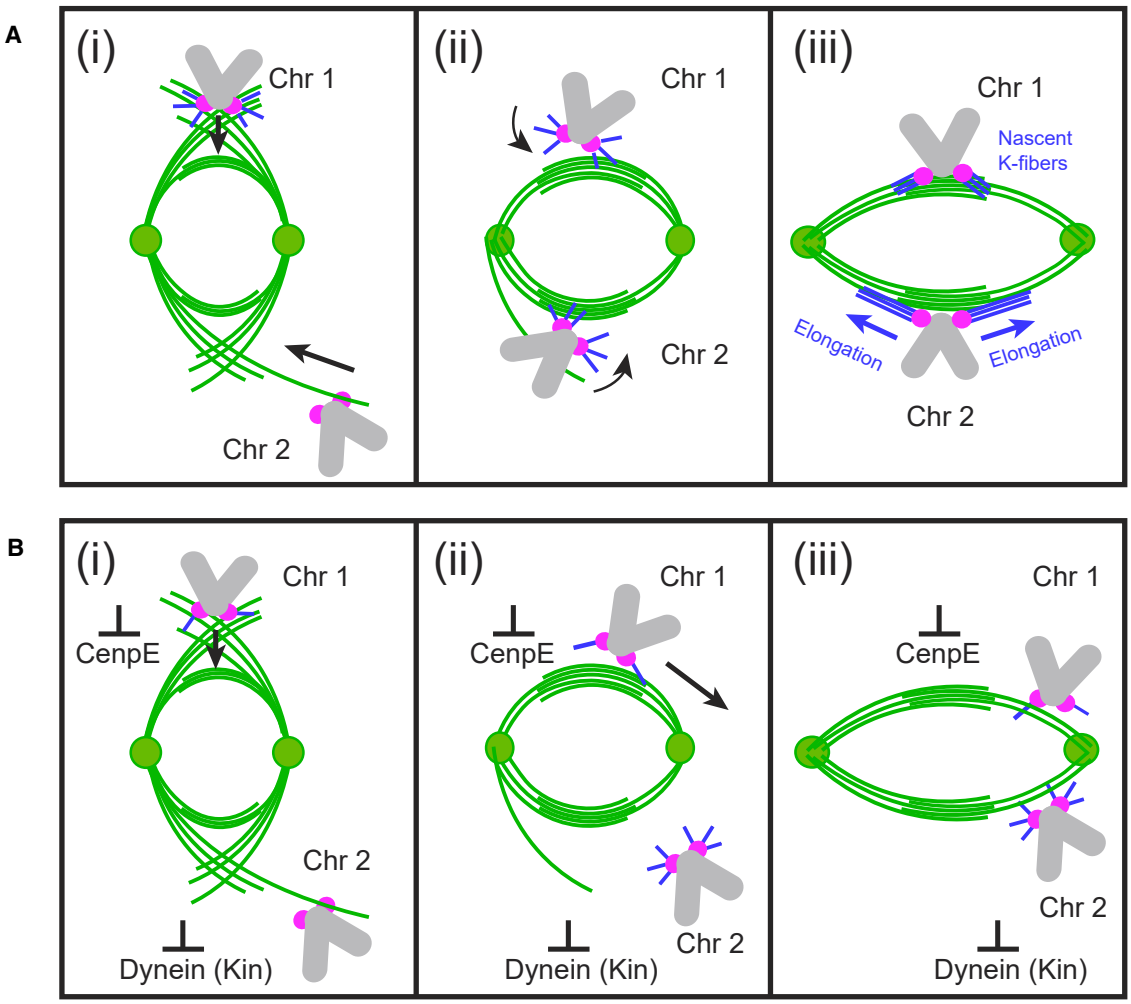


**Figure 7. Centromere behaviors predicted in the model**

(A) Normal mitosis. At early stages of spindle elongation (i) interactions between short MTs at KTs and spindle MTs (Chr1), as well as direct interactions between KTs and astral MTs (Chr2) move centromeres toward the spindle domain enriched with bundles of antiparallel MTs. Both movements are driven by dynein that acts at the minus ends of short MTs (Chr1) or at the KT (Chr2). Near the bundles (ii) dynein-mediated interactions at the minus ends sort MTs protruding from the kinetochores into nascent K-fibers, that support load-bearing connections of sister kinetochores to the opposite spindle poles (iii, Chr1). Nascent K-fibers elongate (iii, Chr2) and their minus ends eventually reach spindle poles.

(B) Effects of abnormal motor activities at KTs. Lower number of MT minus ends protruding from KTs in CenpE-inhibited cells does not significantly interfere with centripetal movement of centromeres on MT arrays with uniform polarity during early prometaphase (i, Chr1); however, sorting of short MTs into nascent K-fibers is impeded (ii, Chr2). As a result, chromosomes congress at the equator but many subsequently shift poleward and become mono-oriented (iii, Chr1). In contrast, absence of dynein at the KT interferes with prompt delivery of peripheral chromosomes to the equatorial zone where antiparallel bundles are numerous (I, Chr2). Encounters with the fully elongated spindle at later times increase the probability of interactions with polarity-biased MT arrays away from the equator, which promotes mono-orientation.

exploration. In some cell types, the force that gathers peripheral chromosomes on the spindle arises from an actin cage.[63–65] This mechanism that acts on the whole spindle would explain the synchrony with which initially scattered chromosomes initiate their movements and arrive at the spindle surface. However, suppression of the rapid inward movement of centromeres observed in $Rod^{\Delta/\Delta}$ cells is more consistent with the notion of KTs gliding alongside captured astral MTs. This movement is known to be driven by dynein bound directly to KTs.[43,47,66,67] Thus, conventional S&C may play an important role during the initial stages by gathering chromosomes in the spindle compartment that supports the nearly synchronous and rapid formation of amphitelic attachments.

## STAR★METHODS

Detailed methods are provided in the online version of this paper and include the following:

- KEY RESOURCES TABLE
- RESOURCE AVAILABILITY
  - Lead contact

## SUPPLEMENTAL INFORMATION

Supplemental information can be found online at https://doi.org/10.1016/j.cub.2022.01.013.

## ACKNOWLEDGMENTS

This work was supported by the National Institutes of Health NIGMS grants GM130298 (A.K.) and GM130234 (T.M.K.). A.M. was supported by the National Science Foundation grant DMS 1953430. L.C. was supported by the Swiss National Science Foundation grant P400PB 183828.

## AUTHOR CONTRIBUTIONS

Conceptualization, F.R., C.M., A.M., and A.K.; methodology, F.R., C.M., A.M., and A.K.; investigation, F.R., I.T., R.F., and L.C.; writing – original draft, F.R., C.M., and A.K., writing – review & editing, F.R., C.M., A.M., T.M.K., and A.K.; supervision, A.K., A.M., and T.M.K.; funding acquisition, A.K., A.M., and T.M.K.

## DECLARATION OF INTERESTS

The authors declare no competing interests.

Received: July 2, 2021
Revised: November 23, 2021
Accepted: January 6, 2022
Published: February 1, 2022

## REFERENCES

1. Kirschner, M., and Mitchison, T. (1986). Beyond self-assembly: from microtubules to morphogenesis. Cell *45*, 329–342.
2. Heald, R., and Khodjakov, A. (2015). Thirty years of search and capture: the complex simplicity of mitotic spindle assembly. J. Cell Biol. *211*, 1103–1111.
3. Petry, S. (2016). Mechanisms of mitotic spindle assembly. Annu. Rev. Biochem. *85*, 659–683.
4. Prosser, S.L., and Pelletier, L. (2017). Mitotic spindle assembly in animal cells: a fine balancing act. Nat. Rev. Mol. Cell Biol. *18*, 187–201.
5. David, A.F., Roudot, P., Legant, W.R., Betzig, E., Danuser, G., and Gerlich, D.W. (2019). Augmin accumulation on long-lived microtubules drives amplification and kinetochore-directed growth. J. Cell Biol. *218*, 2150–2168.
6. Kaláb, P., Pralle, A., Isacoff, E.Y., Heald, R., and Weis, K. (2006). Analysis of a RanGTP-regulated gradient in mitotic somatic cells. Nature *440*, 697–701.
7. Gruss, O.J., Carazo-Salas, R.E., Schatz, C.A., Guarguaglini, G., Kast, J., Wilm, M., Le Bot, N., Vernos, I., Karsenti, E., and Mattaj, I.W. (2001). Ran induces spindle assembly by reversing the inhibitory effect of importin alpha on TPX2 activity. Cell *104*, 83–93.
8. Carazo-Salas, R.E., Gruss, O.J., Mattaj, I.W., and Karsenti, E. (2001). Ran-GTP coordinates regulation of microtubule nucleation and dynamics during mitotic-spindle assembly. Nat. Cell Biol. *3*, 228–234.
9. Kuhn, J., and Dumont, S. (2017). Spindle assembly checkpoint satisfaction occurs via end-on but not lateral attachments under tension. J. Cell Biol. *216*, 1533–1542.
10. Magidson, V., Paul, R., Yang, N., Ault, J.G., O'Connell, C.B., Tikhonenko, I., McEwen, B.F., Mogilner, A., and Khodjakov, A. (2015). Adaptive changes in the kinetochore architecture facilitate proper spindle assembly. Nat. Cell Biol. *17*, 1134–1144.
11. Sacristan, C., Ahmad, M.U.D., Keller, J., Fermie, J., Groenewold, V., Tromer, E., Fish, A., Melero, R., Carazo, J.M., Klumperman, J., et al. (2018). Dynamic kinetochore size regulation promotes microtubule capture and chromosome biorientation in mitosis. Nat. Cell Biol. *20*, 800–810.
12. Rodriguez-Rodriguez, J.A., Lewis, C., McKinley, K.L., Sikirzhytski, V., Corona, J., Maciejowski, J., Khodjakov, A., Cheeseman, I.M., and Jallepalli, P.V. (2018). Distinct roles of RZZ and Bub1-KNL1 in mitotic checkpoint signaling and kinetochore expansion. Curr. Biol. *28*, 3422–3429.e5.
13. Pereira, C., Reis, R.M., Gama, J.B., Celestino, R., Cheerambathur, D.K., Carvalho, A.X., and Gassmann, R. (2018). Self-assembly of the RZZ complex into filaments drives kinetochore expansion in the absence of microtubule attachment. Curr. Biol. *28*, 3408–3421.e8.
14. Renda, F., and Khodjakov, A. (2021). Role of spatial patterns and kinetochore architecture in spindle morphogenesis. Semin. Cell Dev. Biol. *117*, 75–85.
15. Walczak, C.E., Cai, S., and Khodjakov, A. (2010). Mechanisms of chromosome behaviour during mitosis. Nat. Rev. Mol. Cell Biol. *11*, 91–102.
16. Tolić, I.M., and Pavin, N. (2021). Mitotic spindle: lessons from theoretical modeling. Mol. Biol. Cell *32*, 218–222.
17. McIntosh, J.R., Molodtsov, M.I., and Ataullakhanov, F.I. (2012). Biophysics of mitosis. Q. Rev. Biophys. *45*, 147–207.
18. Magidson, V., and Khodjakov, A. (2013). Circumventing photodamage in live-cell microscopy. Methods Cell Biol. *114*, 545–560.
19. Magidson, V., O'Connell, C.B., Lončarek, J., Paul, R., Mogilner, A., and Khodjakov, A. (2011). The spatial arrangement of chromosomes during prometaphase facilitates spindle assembly. Cell *146*, 555–567.
20. Lukinavičius, G., Reymond, L., D'Este, E., Masharina, A., Göttfert, F., Ta, H., Güther, A., Fournier, M., Rizzo, S., Waldmann, H., et al. (2014). Fluorogenic probes for live-cell imaging of the cytoskeleton. Nat. Methods *11*, 731–733.
21. Mollinari, C., Kleman, J.P., Jiang, W., Schoehn, G., Hunter, T., and Margolis, R.L. (2002). PRC1 is a microtubule binding and bundling protein essential to maintain the mitotic spindle midzone. J. Cell Biol. *157*, 1175–1186.
22. Subramanian, R., Wilson-Kubalek, E.M., Arthur, C.P., Bick, M.J., Campbell, E.A., Darst, S.A., Milligan, R.A., and Kapoor, T.M. (2010). Insights into antiparallel microtubule crosslinking by PRC1, a conserved nonmotor microtubule binding protein. Cell *142*, 433–443.
23. Kajtez, J., Solomatina, A., Novak, M., Polak, B., Vukušić, K., Rüdiger, J., Cojoc, G., Milas, A., Šumanovac Šestak, I., Risteski, P., et al. (2016). Overlap microtubules link sister k-fibres and balance the forces on bi-oriented kinetochores. Nat. Commun. *7*, 10298.
24. Jagrić, M., Risteski, P., Martinčić, J., Milas, A., and Tolić, I.M. (2021). Optogenetic control of PRC1 reveals its role in chromosome alignment on the spindle by overlap length-dependent forces. eLife *10*, e61170.
25. Micheva, K.D., and Smith, S.J. (2007). Array tomography: a new tool for imaging the molecular architecture and ultrastructure of neural circuits. Neuron *55*, 25–36.
26. Sikirzhytski, V., Renda, F., Tikhonenko, I., Magidson, V., McEwen, B.F., and Khodjakov, A. (2018). Microtubules assemble near most kinetochores during early prometaphase in human cells. J. Cell Biol. *217*, 2647–2659.

27. Sikirzhytski, V., Magidson, V., Steinman, J.B., He, J., Le Berre, M., Tikhonenko, I., Ault, J.G., McEwen, B.F., Chen, J.K., Sui, H., et al. (2014). Direct kinetochore-spindle pole connections are not required for chromosome segregation. J. Cell Biol. *206*, 231–243.

28. Mollinari, C., Kleman, J.P., Saoudi, Y., Jablonski, S.A., Perard, J., Yen, T.J., and Margolis, R.L. (2005). Ablation of PRC1 by small interfering RNA demonstrates that cytokinetic abscission requires a central spindle bundle in mammalian cells, whereas completion of furrowing does not. Mol. Biol. Cell *16*, 1043–1055.

29. Pamula, M.C., Carlini, L., Forth, S., Verma, P., Suresh, S., Legant, W.R., Khodjakov, A., Betzig, E., and Kapoor, T.M. (2019). High-resolution imaging reveals how the spindle midzone impacts chromosome movement. J. Cell Biol. *218*, 2529–2544.

30. Nunes, V., Dantas, M., Castro, D., Vitiello, E., Wang, I., Carpi, N., Balland, M., Piel, M., Aguiar, P., Maiato, H., and Ferreira, J.G. (2020). Centrosome-nuclear axis repositioning drives the assembly of a bipolar spindle scaffold to ensure mitotic fidelity. Mol. Biol. Cell *31*, 1675–1690.

31. Rieder, C.L., Schultz, A., Cole, R., and Sluder, G. (1994). Anaphase onset in vertebrate somatic cells is controlled by a checkpoint that monitors sister kinetochore attachment to the spindle. J. Cell Biol. *127*, 1301–1310.

32. Maiato, H., Rieder, C.L., and Khodjakov, A. (2004). Kinetochore-driven formation of kinetochore fibers contributes to spindle assembly during animal mitosis. J. Cell Biol. *167*, 831–840.

33. Elting, M.W., Hueschen, C.L., Udy, D.B., and Dumont, S. (2014). Force on spindle microtubule minus ends moves chromosomes. J. Cell Biol. *206*, 245–256.

34. Rusan, N.M., Tulu, U.S., Fagerstrom, C.J., and Wadsworth, P. (2002). Reorganization of the microtubule array in prophase/prometaphase requires cytoplasmic dynein-dependent microtubule transport. J. Cell Biol. *158*, 997–1003.

35. Yildiz, A., Tomishige, M., Gennerich, A., and Vale, R.D. (2008). Intramolecular strain coordinates kinesin stepping behavior along microtubules. Cell *134*, 1030–1041.

36. Khataee, H., and Howard, J. (2019). Force generated by two kinesin motors depends on the load direction and intermolecular coupling. Phys. Rev. Lett. *122*, 188101.

37. Nicklas, R.B., and Koch, C.A. (1969). Chromosome micromanipulation. 3. Spindle fiber tension and the reorientation of mal-oriented chromosomes. J. Cell Biol. *43*, 40–50.

38. Nicklas, R.B., and Ward, S.C. (1994). Elements of error correction in mitosis: microtubule capture, release, and tension. J. Cell Biol. *126*, 1241–1253.

39. Tanaka, T.U., Rachidi, N., Janke, C., Pereira, G., Galova, M., Schiebel, E., Stark, M.J., and Nasmyth, K. (2002). Evidence that the Ipl1-Sli15 (Aurora kinase-INCENP) complex promotes chromosome bi-orientation by altering kinetochore-spindle pole connections. Cell *108*, 317–329.

40. Lampson, M.A., and Cheeseman, I.M. (2011). Sensing centromere tension: Aurora B and the regulation of kinetochore function. Trends Cell Biol. *21*, 133–140.

41. Nicklas, R.B., Waters, J.C., Salmon, E.D., and Ward, S.C. (2001). Checkpoint signals in grasshopper meiosis are sensitive to microtubule attachment, but tension is still essential. J. Cell Sci. *114*, 4173–4183.

42. Chakraborty, M., Tarasovetc, E.V., Zaytsev, A.V., Godzi, M., Figueiredo, A.C., Ataullakhanov, F.I., and Grishchuk, E.L. (2019). Microtubule end conversion mediated by motors and diffusing proteins with no intrinsic microtubule end-binding activity. Nat. Commun. *10*, 1673.

43. Yang, Z., Tulu, U.S., Wadsworth, P., and Rieder, C.L. (2007). Kinetochore dynein is required for chromosome motion and congression independent of the spindle checkpoint. Curr. Biol. *17*, 973–980.

44. Cheerambathur, D.K., Gassmann, R., Cook, B., Oegema, K., and Desai, A. (2013). Crosstalk between microtubule attachment complexes ensures accurate chromosome segregation. Science *342*, 1239–1242.

45. Barisic, M., Aguiar, P., Geley, S., and Maiato, H. (2014). Kinetochore motors drive congression of peripheral polar chromosomes by overcoming random arm-ejection forces. Nat. Cell Biol. *16*, 1249–1256.

46. Wood, K.W., Lad, L., Luo, L., Qian, X., Knight, S.D., Nevins, N., Brejc, K., Sutton, D., Gilmartin, A.G., Chua, P.R., et al. (2010). Antitumor activity of an allosteric inhibitor of centromere-associated protein-E. Proc. Natl. Acad. Sci. USA *107*, 5839–5844.

47. Li, Y., Yu, W., Liang, Y., and Zhu, X. (2007). Kinetochore dynein generates a poleward pulling force to facilitate congression and full chromosome alignment. Cell Res. *17*, 701–712.

48. Karess, R. (2005). Rod-Zw10-Zwilch: a key player in the spindle checkpoint. Trends Cell Biol. *15*, 386–392.

49. Wollman, R., Cytrynbaum, E.N., Jones, J.T., Meyer, T., Scholey, J.M., and Mogilner, A. (2005). Efficient chromosome capture requires a bias in the 'search-and-capture' process during mitotic-spindle assembly. Curr. Biol. *15*, 828–832.

50. Paul, R., Wollman, R., Silkworth, W.T., Nardi, I.K., Cimini, D., and Mogilner, A. (2009). Computer simulations predict that chromosome movements and rotations accelerate mitotic spindle assembly without compromising accuracy. Proc. Natl. Acad. Sci. USA *106*, 15708–15713.

51. Kalinina, I., Nandi, A., Delivani, P., Chacón, M.R., Klemm, A.H., Ramunno-Johnson, D., Krull, A., Lindner, B., Pavin, N., and Tolić-Nørrelykke, I.M. (2013). Pivoting of microtubules around the spindle pole accelerates kinetochore capture. Nat. Cell Biol. *15*, 82–87.

52. Blackwell, R., Sweezy-Schindler, O., Edelmaier, C., Gergely, Z.R., Flynn, P.J., Montes, S., Crapo, A., Doostan, A., McIntosh, J.R., Glaser, M.A., and Betterton, M.D. (2017). Contributions of microtubule dynamic instability and rotational diffusion to kinetochore capture. Biophys. J. *112*, 552–563.

53. Edelmaier, C., Lamson, A.R., Gergely, Z.R., Ansari, S., Blackwell, R., McIntosh, J.R., Glaser, M.A., and Betterton, M.D. (2020). Mechanisms of chromosome biorientation and bipolar spindle assembly analyzed by computational modeling. eLife *9*, e48787.

54. Pavin, N., and Tolić-Nørrelykke, I.M. (2014). Swinging a sword: how microtubules search for their targets. Syst. Synth. Biol. *8*, 179–186.

55. Witt, P.L., Ris, H., and Borisy, G.G. (1980). Origin of kinetochore microtubules in Chinese hamster ovary cells. Chromosoma *81*, 483–505.

56. Snyder, J.A., and McIntosh, J.R. (1975). Initiation and growth of microtubules from mitotic centers in lysed mammalian cells. J. Cell Biol. *67*, 744–760.

57. Kiewisz, R., Fabig, G., Conway, W., Needleman, D., and Müller-Reichert, T. (2021). Three-dimensional structure of the kinetochore-fibers in human mitotic spindles. bioRxiv. https://doi.org/10.1101/2021.11.13.468347.

58. Khodjakov, A., Copenagle, L., Gordon, M.B., Compton, D.A., and Kapoor, T.M. (2003). Minus-end capture of preformed kinetochore fibers contributes to spindle morphogenesis. J. Cell Biol. *160*, 671–683.

59. Tulu, U.S., Fagerstrom, C., Ferenz, N.P., and Wadsworth, P. (2006). Molecular requirements for kinetochore-associated microtubule formation in mammalian cells. Curr. Biol. *16*, 536–541.

60. Nixon, F.M., Honnor, T.R., Clarke, N.I., Starling, G.P., Beckett, A.J., Johansen, A.M., Brettschneider, J.A., Prior, I.A., and Royle, S.J. (2017). Microtubule organization within mitotic spindles revealed by serial block face scanning electron microscopy and image analysis. J. Cell Sci. *130*, 1845–1855.

61. McDonald, K.L., O'Toole, E.T., Mastronarde, D.N., and McIntosh, J.R. (1992). Kinetochore microtubules in PTK cells. J. Cell Biol. *118*, 369–383.

62. O'Toole, E., Morphew, M., and McIntosh, J.R. (2020). Electron tomography reveals aspects of spindle structure important for mechanical stability at metaphase. Mol. Biol. Cell *31*, 184–195.

63. Mogessie, B., and Schuh, M. (2017). Actin protects mammalian eggs against chromosome segregation errors. Science *357*, eaal1647.

64. Booth, A., Jr., Yue, Z., Eykelenboom, J.K., Stiff, T., Luxton, G.W.G., Hochegger, H., and Tanaka, T.U. (2019). Contractile acto-myosin network

on nuclear envelope remnants positions human chromosomes for mitosis. eLife *8*, e46902.

65. Lénárt, P., Bacher, C.P., Daigle, N., Hand, A.R., Eils, R., Terasaki, M., and Ellenberg, J. (2005). A contractile nuclear actin network drives chromosome congression in oocytes. Nature *436*, 812–818.

66. Vorozhko, V.V., Emanuele, M.J., Kallio, M.J., Stukenberg, P.T., and Gorbsky, G.J. (2008). Multiple mechanisms of chromosome movement in vertebrate cells mediated through the Ndc80 complex and dynein/dynactin. Chromosoma *117*, 169–179.

67. Rieder, C.L., and Alexander, S.P. (1990). Kinetochores are transported poleward along a single astral microtubule during chromosome attachment to the spindle in newt lung cells. J. Cell Biol. *110*, 81–95.

68. Subramanian, R., Ti, S.C., Tan, L., Darst, S.A., and Kapoor, T.M. (2013). Marking and measuring single microtubules by PRC1 and kinesin-4. Cell *154*, 377–390.

69. Kendall, J., Liu, Q., Bakleh, A., Krasnitz, A., Nguyen, K.C., Lakshmi, B., Gerald, W.L., Powers, S., and Mu, D. (2007). Oncogenic cooperation and coamplification of developmental transcription factor genes in lung cancer. Proc. Natl. Acad. Sci. USA *104*, 16663–16668.

70. Voets, E., Marsman, J., Demmers, J., Beijersbergen, R., and Wolthuis, R. (2015). The lethal response to Cdk1 inhibition depends on sister chromatid alignment errors generated by KIF4 and isoform 1 of PRC1. Sci. Rep. *5*, 14798.

71. Rieder, C.L., and Cassels, G. (1999). Correlative light and electron microscopy of mitotic cells in monolayer cultures. Methods Cell Biol. *61*, 297–315.

## STAR★METHODS

### KEY RESOURCES TABLE

| REAGENT or RESOURCE | SOURCE | IDENTIFIER |
|---|---|---|
| **Antibodies** | | |
| Mouse monoclonal anti-Tubulin (clone DM1A) | Sigma-Aldrich | Cat# T9026; RRID: AB_477593 |
| Rabbit polyclonal PRC1 | Laboratory of Tarun M Kapoor, The Rockefeller University, New York, NY.[68] | N.C |
| Mouse monoclonal 9G3/Hec1 | Abcam | Cat# ab3613; RRID: AB_303949 |
| Mouse Alexa Fluor 594 | Thermo Fisher Scientific | Cat# A-11032; RRID: AB_2534091 |
| Goat anti-Mouse IgG Alexa Fluor 647 | Thermo Fisher Scientific | Cat# A-21236; RRID: AB_2535805 |
| Goat anti-Rabbit Alexa Fluor 594 | Thermo Fisher Scientific | Cat# A-11012; RRID: AB_141359 |
| Goat anti-Mouse IgG1 ($\gamma$1) Alexa Fluor 488 | Thermo Fisher Scientific | Cat# A-21121; RRID: AB_2535764 |
| Goat anti-Mouse IgG2a Alexa Fluor 594 | Thermo Fisher Scientific | Cat# A-21135; RRID: AB_2535774 |
| **Chemicals, peptides, and recombinant proteins** | | |
| GSK-923295 | MedChemExpress | Cat# HY-10299 |
| PIPES | Sigma-Aldrich | E006757; CAS: 5625-37-6 |
| EGTA | Sigma-Aldrich | E4378; CAS: 67-42-5 |
| $MgCl_2$ | Sigma-Aldrich | CAS 7791-18-6 |
| Triton X-100 | Sigma-Aldrich | X-100; CAS No: 9036-19-5 |
| Glutaraldehyde | Sigma-Aldrich | G5882; CAS: 111-30-8 |
| Paraformaldehyde | Electron Microscopy Sciences | Cat# 15714 |
| EDTA | Sigma-Aldrich | E-5134; CAS: 6381-92-6 |
| Phosphate-buffered saline, pH 7.2 | Thermo Fisher Scientific | Cat# 20012050 |
| Tween 20 | Sigma-Aldrich | P1379; CAS 9005-64-5 |
| Sodium Borohydride | Sigma-Aldrich | 452882; CAS: 16940-66-2 |
| Hoechst 33342 | Molecular Probes | Cat# H3570 |
| $CaCl_2$ | Acros Organics | AC123350025; CAS 10035-04-8 |
| HEPES | Sigma-Aldrich | H4034; CAS 7365-45-9 |
| KCl | Fisher | Cat# P217-3; CAS 7447-40-7 |
| NaCl | Fisher | Cat# S640-3; CAS 7647-14-5 |
| $Na_2HPO_4$ | Sigma | Cat# S374-3; CAS 7558-79-4 |
| Dextrose | Fisher | Cat# BP350–1; CAS 50-99-7 |
| Polybrene | Sigma-Aldrich | Cat# H9268; CAS: 28728-55-4 |
| Blasticidin | InvivoGen | ant-bl-05 |
| Puromycin | Sigma-Aldrich | P7255; CAS 58-58-2 |
| Doxycycline Hyclate | Sigma-Aldrich | D9891; CAS: 24390-14-5 |
| **Critical commercial assays** | | |
| SiR-Tubulin Kit | Spirochrome AG | CY-SC002 |
| Lipofectamine 2000 | ThermoFisher | 11668027 |
| **Deposited data** | | |
| Kinetochore tracking data | This study | https://doi.org/10.5281/zenodo.5803448 |
| **Experimental models: Cell lines** | | |
| Human: hTERT-RPE-1(retinal pigmented epithelium, female) co-expressing CENP-A-GFP and centrin1-GFP | Laboratory of Alexey Khodjakov, Wadsworth Center, New York State Department of Health, Albany, NY.[19] | N/A |
| Human: hTERT-RPE-1 expressing GFP-PRC1 | Laboratory of Tarun M Kapoor, The Rockefeller University, New York, NY.[68] | N/A |
| Human: hTERT-RPE-1 expressing Sh-PRC1 RPE1 | Laboratory of Tarun M Kapoor, The Rockefeller University, New York, NY.[29] | N/A |

(*Continued on next page*)

*Continued*

| REAGENT or RESOURCE | SOURCE | IDENTIFIER |
|---|---|---|
| Human: hTERT RPE KNTC1$^{-/-}$ | Laboratory of Prasad V. Jallepalli, Ioan Kettering Institute, Memorial Sloan Kettering Cancer Center, New York, NY.[12] | N/A |
| Human: hTERT-RPE-1 TetON Sh-PRC1 RPE1 | This study | N/A |
| Human: Ampho-293 (embryonic kidney, female) | Clontech | 631505 |
| Human: hTERT-RPE1 Rod$^{\Delta/\Delta}$ co-expressing CENP-A-GFP and centrin1-GFP | This study | N/A |
| Oligonucleotides | | |
| shRNA targeting sequence: PRC1; 5-GTGATTGAGGCAATTCGAG-3′ | Laboratory of Tarun M Kapoor, The Rockefeller University, New York, NY.[29] | N/A |
| Recombinant DNA | | |
| pMSCVblast vector[69] | Addgene | Addgene # 7508 |
| Software and algorithms | | |
| ImageJ/Fiji | NIH | https://imagej.nih.gov/ij/ |
| MATLAB, R2021a | Mathworks | https://www.mathworks.com |
| Imaris | Oxford Instruments | https://imaris.oxinst.com |
| Adobe Suite CC 2021 | Adobe | https://www.adobe.com |
| SoftWoRx 5.0 | Applied Precision | N/A |
| Simulation code | This study | https://doi.org/10.5281/zenodo.5804405 |

## RESOURCE AVAILABILITY

### Lead contact

Further information and requests for resources and reagents should be directed to and will be fulfilled by the Lead Contact, Alexey Khodjakov (alexey.khodjakov@health.ny.gov).

### Materials Availability

All unique reagents generated in this study are available from the Lead Contact without restrictions.

### Data and code availability

- Kinetochore tracking data have been deposited at Zenodo and are publicly available as of the date of publication. DOI is listed in the key resources table
- Computer simulation code has been deposited at Zenodo and is publicly available as of the date of publication. DOI is listed in the key resources table.
- Any additional information required to reanalyze the data reported in this paper is available from the lead contact upon request.

## EXPERIMENTAL MODEL AND SUBJECT DETAILS

### Cell lines and chemicals

Cell lines used in this study are listed in the key resources table. hTERT RPE1 (human retinal pigment epithelial, female) co-expressing CENP-A-GFP and centrin1-GFP,[19] hTERT RPE1 expressing GFP-PRC1 or Sh-PRC1, hTERT-RPE1 Rod$^{\Delta/\Delta}$ co-expressing CENP-A-GFP and centrin1-GFP cells were maintained in antibiotic-free DMEM/F-12 medium supplemented with 10% fetal bovine serum (FBS, Gibco) at 37 °C, 5% $CO_2$. Culture media for hTERT-RPE1 Rod$^{\Delta/\Delta}$ were additionally supplemented with 1-mM sodium pyruvate (Gibco). Ampho-293 cells (human embryonic kidney, female) were grown in DMEM with 10% FBS and penicillin/streptomycin (Sigma). hTERT RPE1 cells expressing TetON Sh-PRC1 cells were cultured in DMEM with tetracycline-free FSB (Gibco). CenpE was inhibited by 20-nM GSK-923295 (MedChemExpress) added to the growth medium 0.5-2.5 h prior to initiation of live cell recordings of fixation.

## METHOD DETAILS

### Transfection

To generate hTERT-RPE1 Rod$^{\Delta/\Delta}$ cell line with stable expression of CenpA-GFP and Centrin1-GFP, hTERT RPE KNTC1$^{-/-}$ cells,[12] a kind gift from Dr. Prasad V Jallepalli, (Memorial Sloan Kettering Cancer Center), were transfected with lentivirus constructs as previously described.[19]

Constitutive expression of GFP-PRC1 in hTERT RPE1 was achieved by retroviral transduction as previously described.[68] Cells with GFP expression were selected by flow cytometry on a BD FACS Aria system 2 (BD Biosciences) equipped with a 488 nm excitation line and a GFP emission filter.

Two approaches to PRC1 knockdown were utilized. In both, the target sequence 5′-GTGATTGAGGC**A**AT**T**CG**A**G-3′ was used, as it had previously been shown to efficiently knock down PRC1.[69] The shPRC1 construct was generated as previously described[29] and transfected into hTERT RPE1 cells expressing CenpA-GFP and Centrin1-GFP with Lipofectamine 2000 (ThermoFisher). Live-cell recording of these cells were obtained 48-72 h after transfection. In the second approach, we generated cells with tetracycline-inducible expression of the same shRNA construct. The tetracycline repressor sequence was cloned into the pMSCVblast expression vector[70] obtained from Addgene (hereafter 'TetRpMSCVblast'). TetRpMSCVblast construct was first transfected into Ampho-293 cells for retrovirus production. Transfection was performed using the calcium phosphate transfection method. Briefly, a mixture of calcium chloride ($CaCl_2$), TetRpMSCVblast (plasmid DNA) and MilliQ water is made to yield a final concentration of 0.25 M $CaCl_2$ (Acros Organics) and 3 μg of plasmid DNA. A solution of 2X HBS (50 mM HEPES (Sigma), 10 mM KCl (Fisher), 12 mM Dextrose (Fisher), 280 mM NaCl (Fisher),1.5mM $Na_2HPO_4$ (Sigma), pH 7.0) is then added dropwise to the plasmid DNA mixture to yield a 1X HBS mixture, while expelling air from a 2 mL pipette. The final mixture of plasmid DNA and HBS is then added dropwise to ampho-293 cells and incubated overnight. After replacing the medium of transfected cells twice (∼6 and 24 h post transfection), the medium was harvested, passed through a 0.45 μm filter (PALL), and added directly to hTERT-RPE1 cells expressing CenpA-GFP and Centrin1-GFP in the presence of 4 μg/ml polybrene (Sigma). Stable inducible clones were selected with Blasticidin (InvivoGen). Next, the shRNA target sequence in PRC1 was transfected into the inducible clones via retroviral transduction. Clones that stably incorporates the construct were selected with Puromycin (Sigma). For induction of shPRC1, cells were incubated with 5 μg/mL Doxycycline in full growth media 48-72 h prior live-cell recordings.

## Live-cell microscopy

Cells were grown on #1.5 glass coverslips in Petri dishes for 48-72 h. One day prior to the recording, regular culture media was replaced with phenol-red free mixture of DMEM/F-12 containing 10% FBS. Approximately 2 h prior to the recording, coverslips were mounted on Rose chambers and placed on the microscope stage. The chambers were maintained at 37.0 ± 0.3°C within a custom-built enclosure. Imaging was done with a spinning-disc confocal scanner (Yokogawa, X1) attached to a Nikon Ti2E microscope equipped with a λPlanApo 100x1.45 NA oil-immersion objective. 488-nm excitation light intensity was kept at ∼10 nW/μm$^2$ (∼40 μW out of the lens). For tracking KT movements, Z-series of 17-20 sections were collected every 5 s at 100-150 ms exposures and 500-750 nm steps. For shPRC1 RPE1 that display higher variability of mitosis duration, recordings were done at 5-s intervals for the first 20-30 min of prometaphase and at 60-s intervals at later timepoints. The cells were fixed during telophase and immunostained for α-Tubulin. Only cells with no MT bundles and disorganized central spindle were included in the analyses of the KT movements. For recordings of MTs, cells were incubated with 75-nM SiR-Tubulin (Spirochrome, CY-SC002) and 10-μM Verapamil for 2-3 h prior to imaging. 640-nm excitation light intensity was kept at ∼10 nW/μm$^2$ (40 μW out of the lens). All SiR-Tubulin fluorescence recording were done in combination with either CenpA-GFP+Centrin1-GFP or PRC1-GFP at 30-s intervals. All images were captured on a Photometrics 95B Prime camera at 110-nm XY pixel size. The system was controlled by NIS-Elements Imaging Software.

## Fixed-cell immunofluorescence

For MT visualization, cells were pre-extracted in warm PEM buffer (100-mM PIPES, pH 6.9, 2.5-mM EGTA, 5-mM $MgCl_2$) supplemented with 0.5% Triton X-100 for 1 min and fixed with 1% glutaraldehyde in PEM for 10 min. Cells were then stained a monoclonal antibody against α-Tubulin (T9026; Sigma-Aldrich) followed by a secondary antibody conjugated with Alexa Fluor 594 or 647 (Thermo Fisher Scientific).

For PRC1 visualization, cells were pre-extracted in warm PEM buffer (100-mM PIPES pH 7, 1-mM EDTA, 1-mM $MgCl_2$) supplemented with 0.5%Triton X-100 for 30 seconds and fixed with 3.2% paraformaldehyde and 0.1% glutaraldehyde in warm PEM buffer. Cells were then stained with a rabbit polyclonal antibody[29] at 1:1000 followed by a secondary antibody conjugated with Alexa Fluor 594 (Thermo Fisher Scientific). Staining for different antigens was done sequentially. Chromosomes were stained with Hoechst 33343 at 1 μg/ml.

Images of fixed cells were collected on the same microscope as live-cell recordings at 73 or 110-nm XY pixels and 200-nm *Z*-steps. All images were deconvolved with the SoftWoRx 5.0 (Applied Precision) and objective lens-specific point spread function. Precise Axial and Equatorial views of the spindle were generated by rotating the volume in 3-D to orient the spindle axis defined by the 3-D coordinates of both spindle poles.

## Array Tomography

Array Tomography reconstruction were obtained as previously described.[26] KTs and MTs were visualized with monoclonal 9G3/Hec1 (Abcam ab3613) at 1:200 and DM1α antibody (Sigma T9026) antibodies followed by isotype-specific secondary antibodies against mouse γ1 (conjugated to Alexa Fluor 488, Thermo Fisher Scientific, A-21121) and γ2a (conjugated to Alexa Fluor 594, Thermo Fisher Scientific, A-21135). Precise Axial and Equatorial views of the spindle were generated by rotating the volume in 3-D to orient the spindle axis defined by the 3-D coordinates of both spindle poles.

### Correlative Light Electron Microscopy

GFP-PRC1 RPE1 cells were fixed for 30 min in PBS containing 2.5% glutaraldehyde (Sigma-Aldrich). Chromosomes were stained with Hoechst 33342 at 1 μg/ml for 5 min. Complete Z-series were collected as in fixed-cell immunofluorescence preparations. EM embedding and serial sectioning were done as previously described.[71] 80-nm sections were imaged on a JEM 1400 microscope (JEOL) operated at 80 kV using a side-mounted 4.0-megapixel XR401 sCMOS AMT camera (AMT). Complete image series recorded at 8K magnification were used to reconstruct partial volumes containing PRC1 bundles. These volumes were aligned with the light microscopy images by matching positions of chromosome arms. Serial higher-magnification images (40K) were then collected to detail the distribution of the PRC1-decorated microtubule bundles near kinetochores.

## QUANTIFICATION AND STATISTICAL ANALYSIS

### Kinetochore tracking and analysis

KTs and centrioles were detected and tracked in Imaris (Bitplane). Due to a significant number of errors in tracking, particularly at the early stages of spindle assembly, each trajectory was verified and edited by a human operator. Verified trajectories were transferred to Matlab for visualization and analysis.

Temporal synchronization of various recordings was achieved by detecting when spindle elongation is completed in spindle pole trajectories smoothened with the Savitzky-Golay filter over 50 timepoints. The time corresponding to the end of spindle elongation was assigned the value of 1. Progression of time in individual recordings was then normalized to this value. For synchronization of spatial coordinates among multiple cells, all distances were normalized by assigning the value of 1 to the length of the spindle at the timepoint when spindle elongation was completed.

Centromere trajectories were constructed by calculating the center between sister KTs and analyzed in a spindle-centric cylindrical coordinate system, in which, at every time point, the spindle axis is a chosen reference z-axis of the cell 3D space, with the origin in the middle between the centrosomes. A KT position is given by three coordinates: distance along the axis $z$, radial distance $\rho$ from the axis and angular direction $\varphi$ around the axis. In this system, centrosomes simply segregate symmetrically along the straight axis, while movements of centromeres can be conveniently viewed by either projecting their trajectories onto the plane orthogonal to the spindle axis, where we can see $\rho$ and $\varphi$ coordinates but not $z$-coordinates (Figures S3B and S3D, Equatorial), or by plotting $z$ and $\rho$ coordinates (while ignoring $\varphi$ coordinate) on any plane coming through the spindle axis (Figures S3B and S3D, Axial). In this view, $z$ is the horizontal axis, and $\rho$ is the coordinate in the vertical direction of the plane. For convenience, we randomly invert the sign of $\rho$ coordinate for half of trajectories so that the appearance of the plot resembles a spindle.

### Computational model

The computational model describes the dynamic mechanical interactions between short MTs, long MTs, and KTs in two spatial dimensions. At every time step, stochastic binding and unbinding events between short and long MTs are processed via the Gillespie algorithm, then mechanical forces are computed and used to update positions using a Euler-Maruyama integration scheme for stochastic movements. KTs are connected via chromatin, modeled as a Hookean spring force. Short MTs, modeled as stiff springs, emanate from each KT and angularly diffuse while unbound. When bound, molecular motors exert a constant force on minus ends of the short MTs and in the minus-end direction of the bound long MT. Binding occurs with a fixed probability per unit time when the minus-end tip of a short MT tip is in proximity to a long MT. Both ends of the short MTs can unbind. Unbinding from the KT of the plus-end of a short MT occurs at a rate depending on the angle formed with the KT-KT axis, and assuming rapid rebinding at the KT: the short MT is reattached to the KT at a random orientation, keeping the number of short MTs fixed. Unbinding at the minus-end of the short MT is assumed to occur at constant rate. The long MT configurations (geometries and polarities) are fixed in each simulation and modeled with infinite length. The output of the computational model is a time series corresponding to the KT positions, from which the IKD and cTilt angle can be computed and compared to experimentally observed values. Specific equations and computational details are described in Methods S1.

### Characterization of the biorientation domain

To estimate the shape of biorientation domain, 12 recordings of RPE1 cells expressing PRC1-GFP were individually scaled to equalize the maximum length of the spindle among all cells. Each time point in every recording was then rotated to orient the spindle parallel to the abscissa and translated to place the center of the spindle at 0,0,0 coordinates. Maximum-intensity projections were then calculated for each recording and these projections were used to calculate a single average of all 12 recordings. The edge of the domain with high concentration of PRC1-GFP was then empirically matched to a catenary function $y=k*\cosh(x / 1.2)$; where x is spindle length at the timepoint and $k=-1.8*x^{1.2}$.

### Statistical methods

Mean values were compared in the two-tailed heteroscedastic Student's t test. Median values were compared in the Kruskal-Wallis test.

**Current Biology, Volume *32***

## Supplemental Information

# Non-centrosomal microtubules at kinetochores promote rapid chromosome biorientation during mitosis in human cells

**Fioranna Renda, Christopher Miles, Irina Tikhonenko, Rebecca Fisher, Lina Carlini, Tarun M. Kapoor, Alex Mogilner, and Alexey Khodjakov**

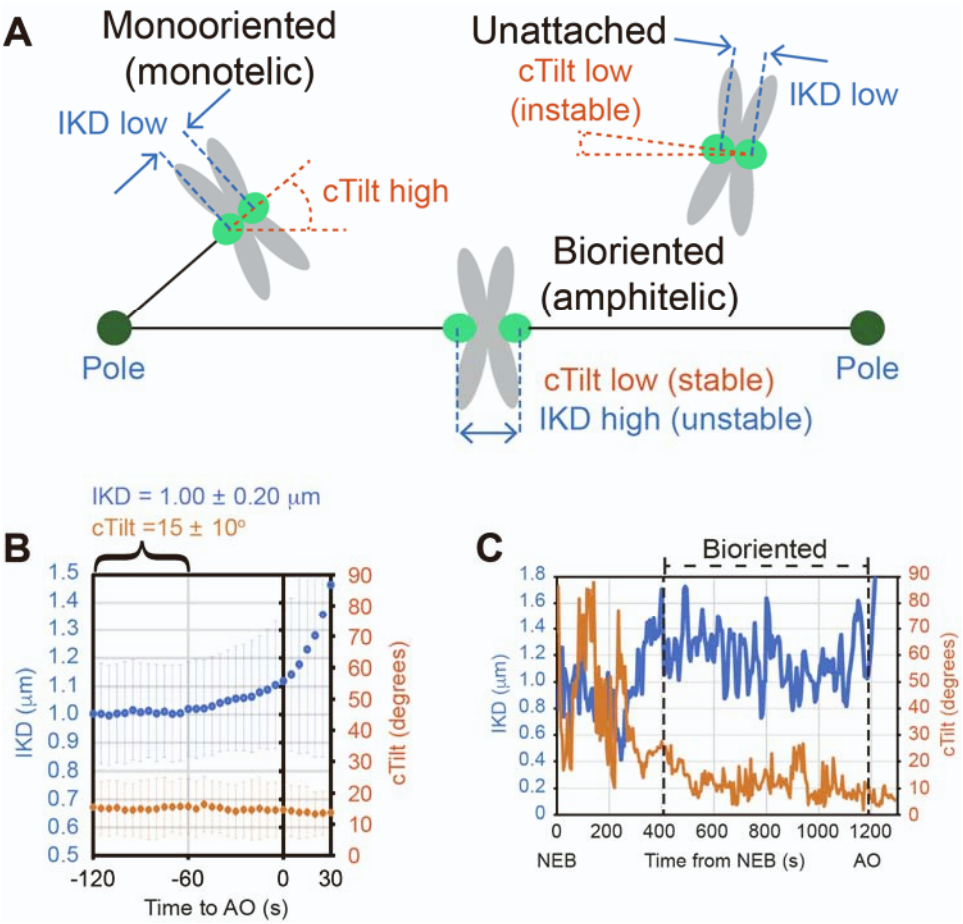


**Figure S1. Criteria for detection of amphitelic attachments in centromere trajectories. Related to Figure 1. (A)** Differences in the centromere orientation and stretching expected for unattached, monooriented, and bioriented chromosomes. Formation of amphitelic attachments leads to poleward pulling forces acting in the opposite directions on sister kinetochores. Thus, biorientation is manifested as an increase in interkinetochore distance (IKD) and a stable decrease of the angle between the centromere axis and spindle axis (centromere tilt, cTilt). **(B)** Mean values of IKD and cTilt observed in RPE1 cells during the two minutes prior to the onset of anaphase (AO) when all chromosomes have formed amphitelic attachments. Error bars are STD. **(C)** Dynamics of IKD and cTilt for a chromosome in RPE1 cell. Dashed lines denote timespan when the chromosome meets the biorientation criteria of IKD > 0.9 μm and cTilt < 22.5°. NEB, nuclear envelope breakdown.

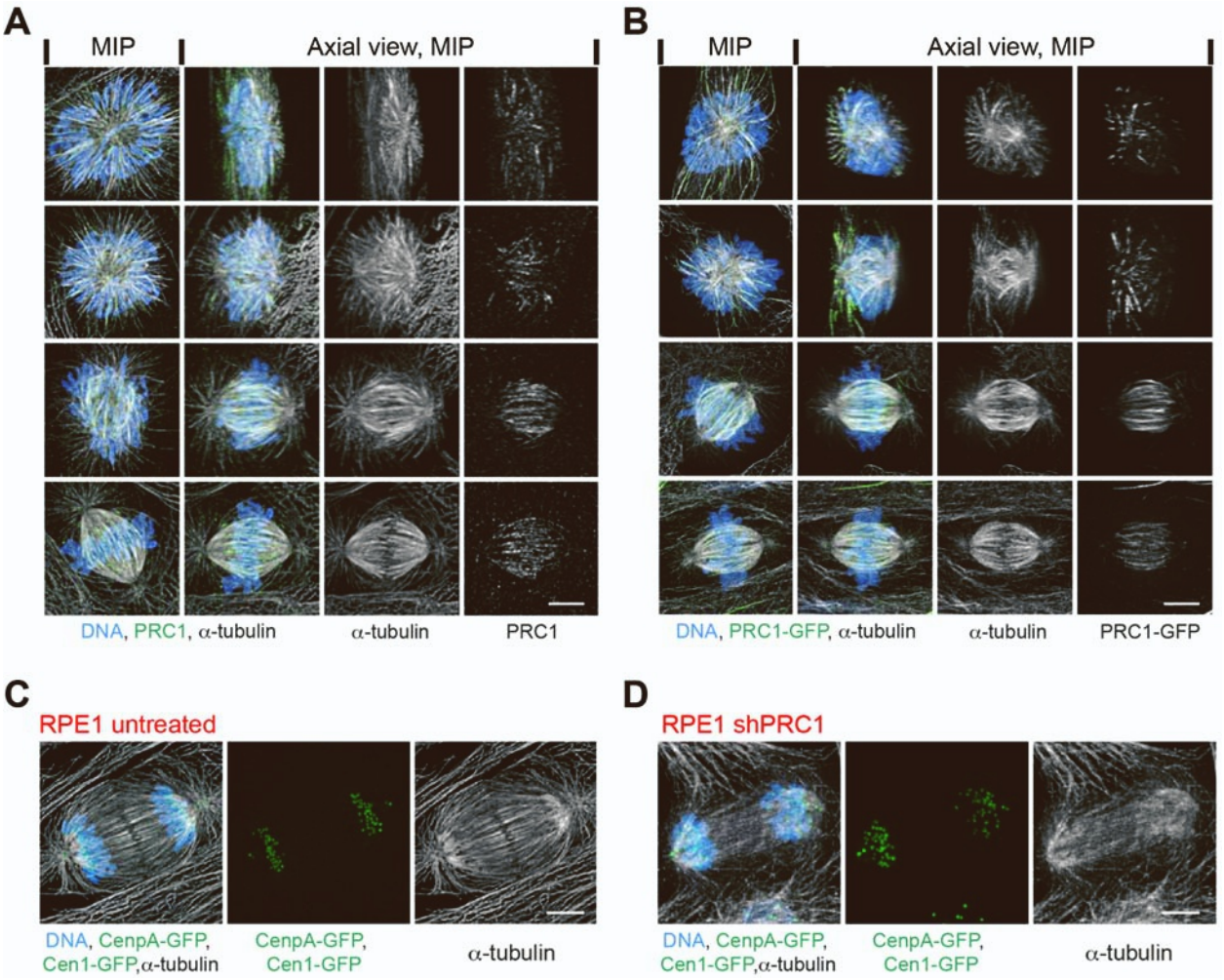


**Figure S2. Distribution of PRC1 at various stages of mitosis and the effect of PRC1 depletion in RPE1 cells. Related to Figures 2 and 3. (A)** Selected cells immuno-stained for microtubules (α-tubulin) and PRC1. Chromosomes are counterstained with Hoechst 33342. All images are maximal-intensity projections of 3-D volumes that include the entire cell. Left column presents cells in their natural orientation. Three right columns present the same volumes rotated to generate a precisely axial view of the spindle. Notice that PRC1-positive bundles form a barrel-shaped structure within the spindle. **(B)** Similar to (A) but the bundles are visualized via constitutive ectopic expression of full-length PRC1-GFP. Notice similarity in the distribution patterns of the endogenous PRC1 (A) and PRC1-GFP (B). **(C-D)** Spindle architecture during telophase in a wild-type RPE1 cell (C) vs. RPE1 cell depleted of PRC1 (D). Notice lack of microtubule bundles in the depleted cell. Timelapse recording of the cell shown in (D) is presented in Video S3 and selected frames from the recording – in Figure 3C. The cell was fixed within seconds after the last recorded timepoint and stained for α-Tubulin. Only cells that lacked microtubule bundles during telophase were selected for analyses of KT movements. Scale bars, 5 μm.

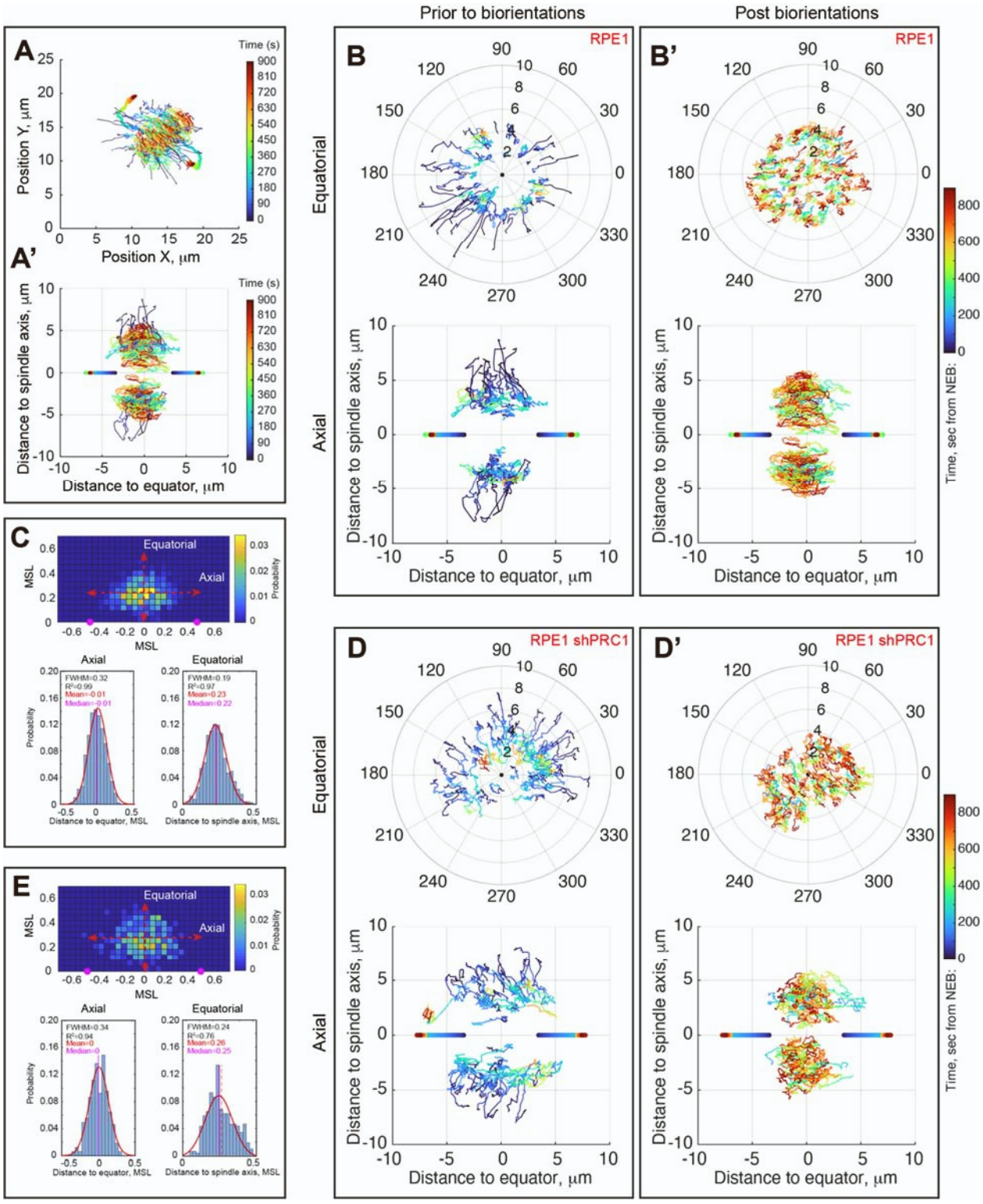


**Figure S3. Methodology for analyses of centromere movements and spatial distribution of biorientation events. Related to Figure 3. (A)** Trajectories of spindle poles (thicker lines) and centromeres (thinner lines) plotted in a Cartesian coordinate system linked to the microscope

stage. Z-coordinates are omitted in this presentation. Color represents time from NEB. **(A')** Same cell as in (A) but the trajectories are plotted in a spindle-centric cylindrical coordinate system comprising $\varphi$, angle to the horizon; $\rho$, distance to spindle axis; and $z$, distance to the equator. For convenience, in Axial views the sign of $\rho$ coordinate is inverted for half of trajectories. This reduces crowding and the appearance of the plot resembles a spindle. Notice that most chromosomes remain near the equator throughout prometaphase. **(B,B')** Centromere trajectories in an untreated RPE1 cell shown from two viewpoints. Each trajectory is split into two segments – from NEB until the formation of amphitelic attachment on this centromere (B) and from the formation of amphitelic attachment until 900 sec after NEB (B'). Notice rapid linear movements of peripheral chromosomes towards the spindle axis prior to the formation of amphitelic attachment (B). Also notice that most chromosomes abruptly change direction of their movement and begin to move parallel to the spindle axis (B'). **(C)** Assessment of the dimensions of the biorientation domain in the wild type RPE1 cells. 1-d Gaussian functions are fit to the Axial and Equatorial distributions of centromere positions at the timepoint of amphitelic attachment formation and Full Width at Half Maximum (FWHM) of these fits calculated. Notice that both distributions are nearly normal $R^2 > 0.95$). **(D,D')** Similar to (B,B') but the cell is depleted of PRC1 (see Figure S2D). Notice that centripetal movements of centromeres prior to the formation of amphitelic attachment do not terminate abruptly but gradually convert into more regular movements along the spindle axis. **(E)** Similar to (C) but in PRC1-depleted RPE1 cells. Notice that changes in the Axial distribution are less prominent than in the Equatorial. The latter is not normal and positively skewed, indicating a high frequency of amphitelic attachment formations in at larger distances from the spindle axis.

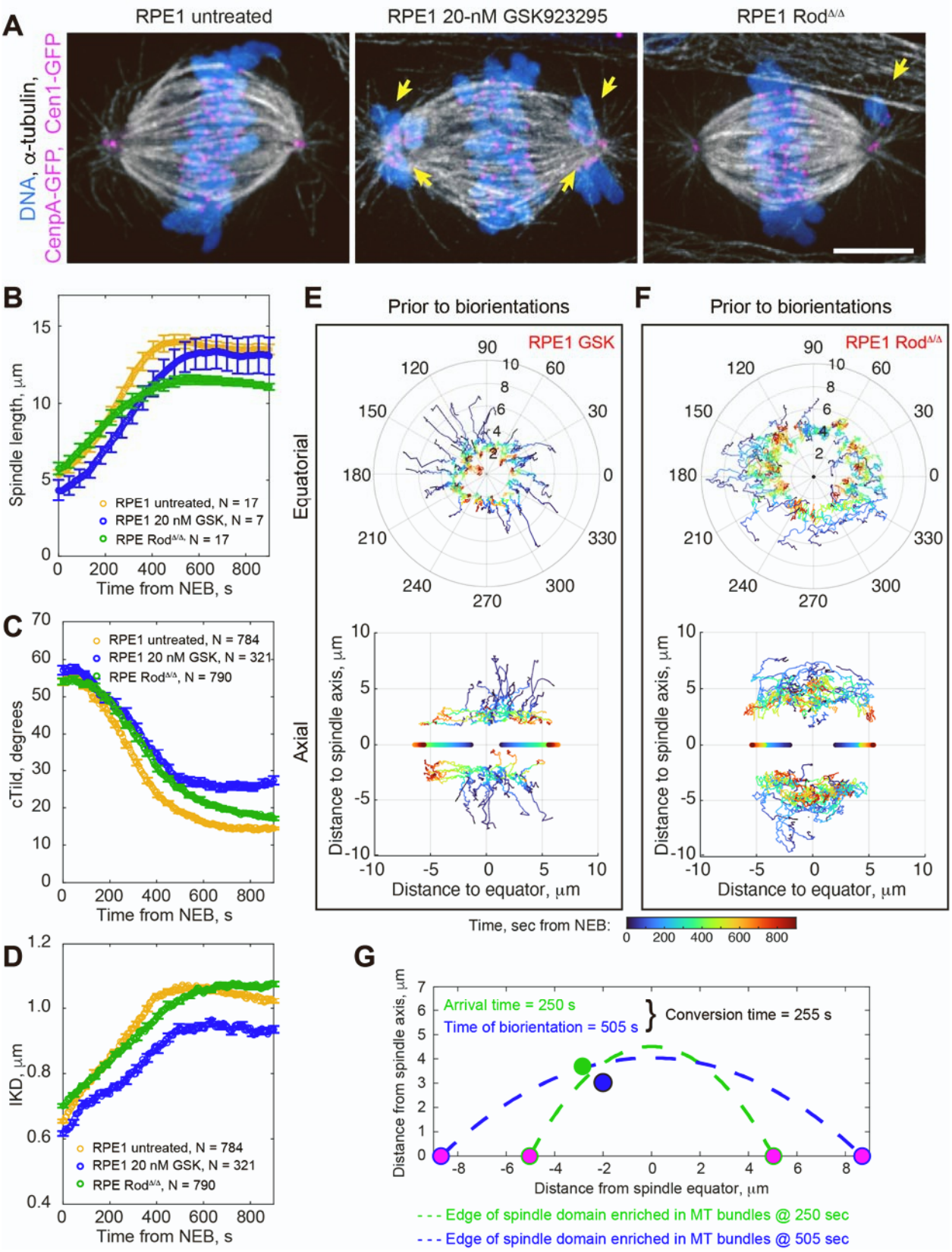
A
RPE1 untreated
RPE1 20-nM GSK923295
RPE1 Rod$^{\Delta/\Delta}$
DNA, α-tubulin,
CenpA-GFP, Cen1-GFP
B
Spindle length, μm
Time from NEB, s
RPE1 untreated, N = 17
RPE1 20 nM GSK, N = 7
RPE Rod$^{\Delta/\Delta}$, N = 17
C
cTild, degrees
Time from NEB, s
RPE1 untreated, N = 784
RPE1 20 nM GSK, N = 321
RPE Rod$^{\Delta/\Delta}$, N = 790
D
IKD, μm
Time from NEB, s
RPE1 untreated, N = 784
RPE1 20 nM GSK, N = 321
RPE Rod$^{\Delta/\Delta}$, N = 790
E
Prior to biorientations
RPE1 GSK
Equatorial
Axial
Distance to spindle axis, μm
Distance to equator, μm
F
Prior to biorientations
RPE1 Rod$^{\Delta/\Delta}$
Distance to spindle axis, μm
Distance to equator, μm
Time, sec from NEB:
G
Distance from spindle axis, μm
Arrival time = 250 s
Time of biorientation = 505 s
Conversion time = 255 s
Distance from spindle equator, μm
- - - Edge of spindle domain enriched in MT bundles @ 250 sec
- - - Edge of spindle domain enriched in MT bundles @ 505 sec

**Figure S4. Spindle assembly and centromere trajectories in cells lacking CenpE- or dynein activity at the kinetochore. Related to Figure 6. (A)** Principal components of the spindle during late prometaphase in the evaluated experimental conditions. Notice monooriented chromosomes (arrows) adjacent to spindle poles in cells with inhibited CenpE (RPE1 20-nM GSK923295) and in cells that lack dynein at the kinetochores (RPE1 $Rod^{\Delta/\Delta}$). Scale bar, 5 μm. **(B-D)** Dynamics of spindle elongation, cTilt, and IKD. Notice similar duration of spindle elongation in all three classes although the maximum length of the spindle in $Rod^{\Delta/\Delta}$ is significantly shorter than in the other two classes (B; $p < 0.001$ in Student's T-test). cTilt decreases at lower rates in CenpE-inhibited and $Rod^{\Delta/\Delta}$ cells (C). The final mean values reached 900 s after NEB are similar in the wild-type and $Rod^{\Delta/\Delta}$ RPE1 but is significantly higher in CenpE-inhibited cells (C). IKD increases significantly slower in CenpE-inhibited cells, and it plateaus at a lower lever in CenpE-inhibited cells (D; $p < 0.001$ in Student's T-test). Difference between the wild-type and $Rod^{\Delta/\Delta}$ RPE1 cells are not significant. Error bars, shown for every $10^{th}$ timepoint, are Standard Error of Mean. **(E,F)** Centromere trajectories prior to the formation of amphitelic attachments in a CenpE-inhibited (E) and in a $Rod^{\Delta/\Delta}$ RPE1 cell (F). Notice that rapid linear movements towards the spindle axis are present in CenpE-inhibited (E) but absent in $Rod^{\Delta/\Delta}$ cells (F). Also notice poleward movement of centromeres along the spindle axis during later stages of prometaphase (color-coded cyan to red) in (E, Axial) and during earlier stages of prometaphase (color-coded blue to cyan) in (F, Axial). **(G)** Methodology for assessing when a centromere is delivered to the biorientation domain, and the time required for the formation of amphitelic attachment within the domain. Green and blue dash lines are catenaries that mark the edge of the spindle domain enriched in microtubule bundles (Figure 4B and Methods) at two timepoints. Green dot denotes position of the centromere at the time point when the Euclidian distance to the contemporary catenary decreases to <0.85 μm for the first time. Blue dot denotes position of the same centromere when formation of amphitelic attachment is detected. Conversion time is the time lapsed from the arrival to amphitelic attachment formation.

# Simulation details

The computational model describes the dynamic mechanical interactions between short microtubules, long microtubules, and kinetochores in two spatial dimensions. All positions described below are 2-dimensional. The coordinate system is assumed to be in the spindle frame, meaning the first component is along the spindle axis and the second component orthogonal to this axis.

## Simulation overview

The following dynamic quantities are tracked in the simulations and updated at each time step.

1. The spatial positions of each kinetochore, $x_1, x_2$, labeled arbitrarily. This allows for the computation of IKD and cTilt,

$$\begin{aligned} \text{IKD} &= \| x_1 - x_2 \| \\ \text{cTilt} &= \arccos\big((x_1 - x_2) \cdot e_1\big) / \| x_1 - x_2 \|, \end{aligned}$$

   where $e_1 = [1,0]$, the unit vector corresponding to the spindle axis.

2. The spatial positions of $S$ minus-end tips of short microtubules emanating from each kinetochore, $y_j^i$ for $j = 1, \dots, S$ and $i = 1,2$.

3. The state of minus-end tips of $S$ short microtubules emanating from each kinetochore, $q_j^i$ for $j = 1, \dots, S$ and $i = 1,2$. The state is either $q = b$ for bound or $q = b$ for bound to a particular long microtubule.

The long microtubules are considered to be static and infinitely long in the simulation, each determined by a point on the line and the plus-end orientation $\phi$. Note that the orientation dictates the polarity of the microtubule. For example, $\phi = 0$ and $\phi = \pi$ are antiparallel, that is, geometrically parallel with opposite polarity.

The time step of simulation, $\Delta t$, is fixed. The initial conditions are taken to be $\mathrm{IKD} = L_{\mathrm{spring}}$ and $\mathrm{cTilt}$ uniformly random. All short microtubules are initially in the unbound state and placed at positions uniformly radial to each kinetochore at distance $L_{\mathrm{short}}$.

Each timestep of the simulation contains two steps:

4. Process binding and unbinding events by calculating position-dependent rates and then simulating whether an event occurs, updating the appropriate states if so.
5. Compute mechanical forces based on positions and use these to update positions

Due to the dependence between the reaction rates and positions, time steps are chosen to be small, and rates are assumed to be constant within each time step. We will describe each of these sub-steps in further detail.

## Binding and unbinding

At each timestep, the rate of each possible reaction is computed based on current positions and states. These reactions are modeled as a Poisson process, where the probability of reaction with rate $\omega$ occuring in a small timestep $[t, t + \Delta t]$ is $p_{\mathrm{react}} = \omega \cdot \Delta t$.

### Binding

Binding can occur when a short MT tip is unbound and near a long microtubule. The binding rate between short MT tip $j$ and long microtubule $k$ is

$$k_{\mathrm{on}}^{j \to k} = \begin{cases} \omega_{\mathrm{on}} & \| y_j - d_k \| \leq R \\ 0 & \text{otherwise,} \end{cases}$$

where $d_k$ is the smallest distance from $y_j$ to the line characterized by $d_k$'s position and direction. In practice, this is straightforward to compute by projection.

In words, binding occurs at constant when the short MT tip is within radius $R$ of a long microtubule. The result of the binding event is that the state $q_j \to b$ and the position is fixed to the closest point on the microtubule $y_j \to d_k$.

**Unbinding**

There are two types of unbinding considered in the model. One is the short MT unbinding at its minus-end from a long MT and the other is unbinding at its plus end from the kinetochore, both only occurring when the short MT is bound on the plus end.

**Type 1 unbinding (plus-end from KT)**. The connection between short MTs and kinetochores is assumed to be dynamic and able to be broken. The rate at which this connection breaks is modeled to depend on the angle between the kinetochore and the short MT, stemming from the assumption that the physical connection would become strained at large angles[S1,S2].

For short MT $j$ bound to kinetochore $i$, this angle is measured by

$$\gamma_j^i = \frac{\left(y_i^j - x_i\right) \cdot \left(x_i - x_{ii}\right)}{\| \, y_i^j - x_i \, \| \| \, x_i - x_{ii} \, \|}.$$

Here $ii$ corresponds to the other kinetochore index. Then, the unbinding rate is a monotonically increasing function of $\gamma$,

$$k_{\text{break}} = \omega_b\left[\tanh\left(-\alpha\gamma_j^i\right) + 1\right].$$

In words, if $\gamma \approx 1$, the short MT emenates straight out of the kinetochore, assumed to be the most stable connection. As mechanics occur, $\gamma \approx 0$ means that the short MT is orthogonal to the kinetochore and this connection breaks with dramatically increased frequency. Short MTs that are connected toward the kinetochore detach effectively immediately, as this is physically unrealistic. The $\alpha$ parameter controls the sensitivity of this mechanism to the angle. When this occurs, $q_j \to u$ and $y_j$ is placed at a uniformly random location $L_{\text{short}}$ distance away from the

kinetochore. That is, a new connection forms immediately and total number of short MTs is conserved. This assumption is justified if the number of short MT connections at the kinetochore interface is limited by the number of linkers.

**Type 2 unbinding (minus-end from long MT)**. The other type of unbinding corresponds to the minus-end of short MT $j$ unbinding from a long microtubule. Although this connection is assumed to be by a molecular motor whose unbinding rate is known to be force-dependent, we assume that the motor force relaxes quickly relative to the rest of the system and this becomes effectively constant,

$$k_{\text{off}} = \omega_{\text{off}}.$$

When this occurs, $q_j^i \to u$ and the position is maintained $y_j^i \to y_j^i$, allowing for the possibility of rebinding quickly after.

## Forces

The force between kinetochores is modeled as a spring with some stiffness and rest length. The force on kinetochore $i$ is

$$F_{\text{spring}}^i = \begin{cases} -k_{\text{spring}}\left(\| x_i - x_{ii} \| - L_{\text{spring}}\right)\dfrac{x_i - x_{ii}}{\| x_i - x_{ii} \|} & \| x_i - x_{ii} \| > L_{\text{spring}} \\ 0 & \text{otherwise.} \end{cases}$$

Rigid short microtubules are modeled as stiff springs, with a nearly fixed length enforced by the spring stiffness.

$$F_{\text{short},j}^i = -k_{\text{short}}\left(\| y_j^i - x_i \| - L_{\text{short}}\right)\frac{y_j^i - x_i}{\| y_j^i - x_i \|}.$$

Effectively an angular spring, we assume there is a force causing short MTs to maintain emanating an angle straight out of kinetochores. Since the tip is modeled as a point, this is

modeled as a force pulling the tip to the position $L_{\text{short}}$ distance away from the kinetochore in the direction of the KT-KT vector. Therefore, the angular force is

$$F^i_{\text{ang},j} = -k_{\text{ang}}\left[y^i_j - \left(x_i + L_{\text{short}}\frac{x_i - x_{ii}}{\| x_i - x_{ii} \|}\right)\right].$$

While bound, the motors exert a constant force $F_m$ on the tip of short MT $j$ in the minus-end direction of the long microtubule described by the unit vector in the direction $-\phi$

$$F^i_{\text{mot},j} = F_m e_{-\phi}.$$

The evolution of the kinetochores due to the forces exerted on it is described by the stochastic differential equation (SDE)

$$\eta_k \dot{x}_i = F^i_{\text{spring}} - \sum_{j=1}^{S} F^i_{\text{short},j} + \xi_k \zeta_i(t),$$

where $\zeta_i$ is a white-noise process corresponding to random fluctuations with magnitude controlled by $\xi_k$ and $\eta_k$ is the effective drag coefficient.

The short microtubule tips follow a similar evolution,

$$\eta_s \dot{y}^j_i = F^i_{\text{short},j} + F^i_{\text{ang},j} + 1_{q^i_j = b} F^i_{\text{mot},j} + \xi_s \zeta_{j,i}(t).$$

where $1.$ is an indicator function causing the motor force to only be exerted while bound. The SDEs are updated at each time step using the Euler-Maruyama scheme.

## Long MT configurations

In the main text, four long MT configurations are mentioned and elaborated upon here. In all configurations, the number long MTs is chosen to be large enough that no simulation reaches a boundary in the timeframe of 100 seconds. That is, the pattern is effectively periodic in both dimensions.

**Antiparallel uniform**. In this configuration, all microtubules are equidistant, with distance $D_1$, in the 2nd dimension and are infinitely long in the first. The orientation alternates between $\phi = 0$ and $\phi = \pi$.

**Antiparallel bundled**. $B$ (an even number) of microtubules within a bundle are equidistant with distance $D_2$ apart from one another, again with alternating $\phi = 0, \pi$ orientation, so the number of each polarity is equal in each bundle. The bundles are placed so that the centers of each bundle at a distance $D_1$ apart.

**Angled**. Reference positions (intercepts) of each microtubule are placed at $(0, z)$ where each $z$ is $D_1$ distance apart. The orientations are then chosen to alternate between $\phi = \pi/4$ and $\phi = -pi/4$, resulting in a square lattice of microtubules.

**Biased bundled**. $B$ (an even number) of microtubules within a bundle are equidistant with distance $D_2$ apart from one another. For a bias $b$, each microtubule is individually assigned $\phi = 0$ with probability $b$ or $\phi = \pi$ with probability $1 - b$. For instance, the $3{:}\,1$ ratio corresponds to $b = 1/4$ (or $3/4$ by symmetry of the model).

## Parameters

Many of the parameters in the computational model have been measured experimentally, although some with reported values spanning several orders of magnitude. In these cases, we chose values roughly in the middle of the range of values. The parameters chosen for simulations can be found in the table below.

Parameters relating to molecular motors and mechanical properties of the kinetochores are thoroughly measured. Parameters that increase the motor attachment rate or force generation lead to faster biorientation. Parameters relating to short microtubules are relatively unknown. Rough estimates regarding number and geometry were made from previous studies, but

mechanical interactions are completely unknown. The plots shown below present parameter sweeps over the unknown short microtubule parameters. Although the biorientation times do depend on each of these parameters, these timings are robust to an order of magnitude when varying each of these parameters by several.

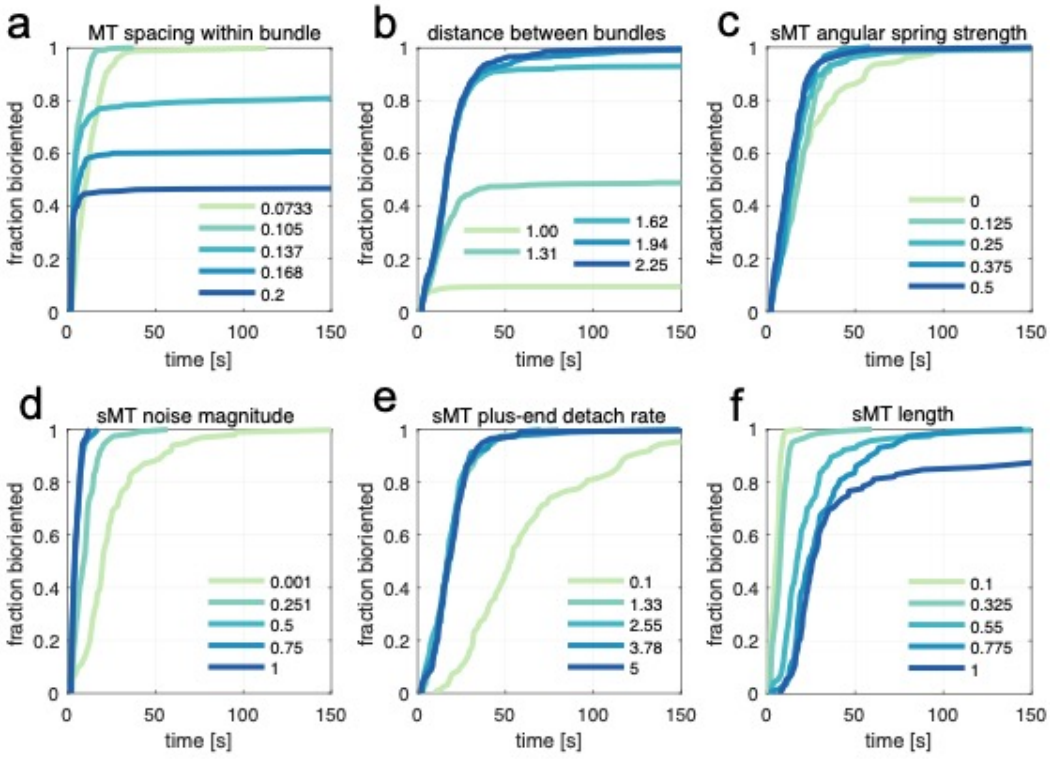


**Plots of additional parameter sweeps showing the dependence on various model parameters for biorientation times**. **a:** Biorientation becomes optimal values of intrabundle spacing, $D_2$, in the relevant on the order of 100 nanometers. **b:** Biorientation becomes favorable for more separated bundles, parameterized by the distance $D_1$. **c:** The angular spring stiffness $k_{\text{spring}}$ has little effect on the biorientation but does facilitate it slightly. **d:** More short microtubule fluctuations, parameterized by $\xi_s$ is favorable for biorientation. **e:** Short microtubules detaching at their plus end, the rate of which is parameterized by $\omega_b$ is necessary for

biorientation but does not improve the rate when made larger. **f:** Shorter short MTs, $L_{\mathrm{short}}$, are favorable for biorientation for the bundled configuration of long MTs only. In uniform (not shown), $L_{\mathrm{short}}$ on the order of hundreds of nanometers is optimal.

## Model parameters

| parameter | meaning | value(s) used in simulation | notes |
|---|---|---|---|
| $S$ | number of short MTs at each KT | varied, 0-40 | estimated from ref[S3] |
| $\omega_{\mathrm{on}}$ | binding rate | 10 $s^{-1}$ | notoriously difficult to measure, estimated magnitude from other motors[S4] |
| $R$ | binding radius | 75 nm | magnitude from dynein stalk length[S5] |
| $\omega_b$ | short MT plus-end breakage rate | 10 $s^{-1}$ | estimated to be on the timescale of motors unbinding |
| $\alpha$ | short MT plus-end breakage angular sensitivity | 100 | unknown, little effect on model behavior |
| $\omega_{\mathrm{off}}$ | short MT minus-end unbinding rate | 1 $s^{-1}$ | magnitude dynein unbinding rate under load[S6,S7] |
| $k_{\mathrm{spring}}$ | KT-KT spring stiffness | 60 pN/$\mu$m | magnitude from[S8-S10] |
| $L_{\mathrm{spring}}$ | KT-KT spring rest length | 0.65 $\mu$m | estimated from data |
| $k_{\mathrm{short}}$ | short MT stiffness | 500 pN/$\mu$m | approximately rigid[S11] |
| $L_{\mathrm{short}}$ | short MT length | 0.5 $\mu$m | estimated from ref[S3] |
| $k_{\mathrm{ang}}$ | short MT angular spring stiffness | 0.2 pN/$\mu$m | unknown |
| $F_m$ | short MT minus-end motor force | 3 pN | magnitude of force exerted by team of dynein |
| $\eta_k$ | kinetochore effective drag coefficient | 30 s·pN/$\mu$m | estimated from ref[S12-S14] |
| $\eta_s$ | short MT effective drag coefficient | 2 s·pN/$\mu$m | estimated as an order of magnitude smaller than KT drag coefficient |
| $\xi_k$ | kinetochore noise magnitude | 0.01 pN· $\mu$m | estimated, taken to be larger than thermal fluctuations alone, little effect on model behavior |
| $\xi_s$ | short MT tip noise magnitude | 0.1 pN· $\mu$m | unknown, estimated |
| $D_1$ | distance between long MT bundles | varied, ~2 $\mu$m | estimated[S11] |
| $D_2$ | distance between long MTs within bundles | varied, ~50 nm | estimated |
| $B$ | number of long MTs within bundle | varied, ~10 | estimated |
| $\Delta t$ | simulation time step | $10^{-3}$ | |

## Supplemental References


S1. Khataee, H., and Howard, J. (2019). Force Generated by Two Kinesin Motors Depends on the Load Direction and Intermolecular Coupling. Phys Rev Lett *122*, 188101. 10.1103/PhysRevLett.122.188101.

S2. Pyrpassopoulos, S., Shuman, H., and Ostap, E.M. (2020). Modulation of Kinesin's Load-Bearing Capacity by Force Geometry and the Microtubule Track. Biophys J *118*, 243-253. 10.1016/j.bpj.2019.10.045.

S3. Sikirzhytski, V., Renda, F., Tikhonenko, I., Magidson, V., McEwen, B.F., and Khodjakov, A. (2018). Microtubules assemble near most kinetochores during early prometaphase in human cells. J Cell Biol *217*, 2647-2659. 10.1083/jcb.201710094.

S4. Leduc, C., Campas, O., Zeldovich, K.B., Roux, A., Jolimaitre, P., Bourel-Bonnet, L., Goud, B., Joanny, J.F., Bassereau, P., and Prost, J. (2004). Cooperative extraction of membrane nanotubes by molecular motors. Proc Natl Acad Sci U S A *101*, 17096-17101. 10.1073/pnas.0406598101.

S5. Can, S., Lacey, S., Gur, M., Carter, A.P., and Yildiz, A. (2019). Directionality of dynein is controlled by the angle and length of its stalk. Nature *566*, 407-410. 10.1038/s41586-019-0914-z.

S6. Kunwar, A., Tripathy, S.K., Xu, J., Mattson, M.K., Anand, P., Sigua, R., Vershinin, M., McKenney, R.J., Yu, C.C., Mogilner, A., and Gross, S.P. (2011). Mechanical stochastic tug-of-war models cannot explain bidirectional lipid-droplet transport. Proc Natl Acad Sci U S A *108*, 18960-18965. 10.1073/pnas.1107841108.

S7. Tan, R., Foster, P.J., Needleman, D.J., and McKenney, R.J. (2018). Cooperative Accumulation of Dynein-Dynactin at Microtubule Minus-Ends Drives Microtubule Network Reorganization. Dev Cell *44*, 233-247 e234. 10.1016/j.devcel.2017.12.023.

S8. Banigan, E.J., Chiou, K.K., Ballister, E.R., Mayo, A.M., Lampson, M.A., and Liu, A.J. (2015). Minimal model for collective kinetochore-microtubule dynamics. Proc Natl Acad Sci U S A *112*, 12699-12704. 10.1073/pnas.1513512112.

S9. Sarangapani, K.K., Akiyoshi, B., Duggan, N.M., Biggins, S., and Asbury, C.L. (2013). Phosphoregulation promotes release of kinetochores from dynamic microtubules via multiple mechanisms. Proc Natl Acad Sci U S A *110*, 7282-7287. 10.1073/pnas.1220700110.

S10. Stephens, A.D., Haase, J., Vicci, L., Taylor, R.M., 2nd, and Bloom, K. (2011). Cohesin, condensin, and the intramolecular centromere loop together generate the mitotic chromatin spring. The Journal of Cell Biology *193*, 1167-1180. 10.1083/jcb.201103138.

S11. Letort, G., Nedelec, F., Blanchoin, L., and Thery, M. (2016). Centrosome centering and decentering by microtubule network rearrangement. Mol Biol Cell *27*, 2833-2843. 10.1091/mbc.E16-06-0395.

S12. Marshall, W.F., Marko, J.F., Agard, D.A., and Sedat, J.W. (2001). Chromosome elasticity and mitotic polar ejection force measured in living Drosophila embryos by four-dimensional microscopy-based motion analysis. Curr Biol *11*, 569-578.

S13. Nicklas, R.B. (1965). Chromosome Velocity during Mitosis as a Function of Chromosome Size and Position. J Cell Biol *25*, SUPPL:119-135. 10.1083/jcb.25.1.119.

S14. Nicklas, R.B. (1988). The forces that move chromosomes in mitosis. Annual Review of Biophysics & Biophysical Chemistry *17*, 431-449.